Citation for final published version:

Zareie, Pirooz, Szeto, Christopher, Farenc, Carine, Gunasinghe, Sachith D., Kolawole, Elizabeth M., Nguyen, Angela, Blyth, Chantelle, Sng, Xavier Y. X., Li, Jasmine, Jones, Claerwen M., Fulcher, Alex J., Jacobs, Jesica R., Wei, Qianru, Wojciech, Lukasz, Petersen, Jan, Gascoigne, Nicholas R.J., Evavold, Brian D., Gaus, Katharina, Gras, Stephanie, Rossjohn, Jamie and La Gruta, Nicole L. 2021. Canonical T cell receptor docking on peptide–MHC is essential for T cell signaling. Science 372 (6546) , eabe9124. 10.1126/science.abe9124

Publishers page: http://dx.doi.org/10.1126/science.abe9124

Canonical T cell Receptor Docking on peptide–MHC is essential for T cell signaling

Pirooz Zareie[1], Christopher Szeto[1#], Carine Farenc[1], Sachith D. Gunasinghe[2], Elizabeth M. Kolawole[3], Angela Nguyen[1], Chantelle Blyth[1], Xavier Y. X. Sng[1], Jasmine Li[4], Claerwen M. Jones[1], Alex J. Fulcher[5], Jesica R. Jacobs[3], Qianru Wei[6], Lukasz Wojciech[6], Jan Petersen[1,7], Nicholas R.J. Gascoigne[6], Brian D. Evavold[3], Katharina Gaus[2], Stephanie Gras[1,7*#], Jamie Rossjohn[1,7,8*] & Nicole L. La Gruta[1*]

[1]Infection and Immunity Program and Department of Biochemistry and Molecular Biology, Biomedicine Discovery Institute, Monash University, Clayton, VIC, Australia.

[2]European Molecular Biology Laboratory (EMBL) Australia Node in Single Molecule Science and the ARC Centre of Excellence in Advanced Molecular Imaging, School of Medical Sciences, University of New South Wales, NSW, Australia.

[3]Department of Pathology, University of Utah School of Medicine, Salt Lake City, UT, USA.

[4]Infection and Immunity Program and Department of Microbiology, Biomedicine Discovery Institute, Monash University, Clayton, VIC, Australia.

[5]Monash Micro Imaging, Monash University, Clayton, VIC, Australia.

[6]Immunology Programme and Department of Microbiology and Immunology, Yong Loo Lin School of Medicine, National University of Singapore, Singapore 117545.

[7]Australian Research Council Centre of Excellence in Advanced Molecular Imaging, Monash University, Clayton, VIC, Australia.

[8]Institute of Infection and Immunity, Cardiff University School of Medicine, Heath Park, Cardiff, UK.

[#] Current address: Department of Biochemistry and Genetics, La Trobe Institute for Molecular Science, La Trobe University, Melbourne, Victoria, Australia

[*]Joint senior and corresponding authors: Nicole.la.gruta@monash.edu, Jamie.rossjohn@monash.edu, S.gras@latrobe.edu.au

Abstract

T cell receptor (TCR) recognition of peptide–major histocompatibility complexes (pMHCs) is characterized by a highly conserved docking polarity. Whether this polarity is driven by recognition or signaling constraints remains unclear. Using "reversed docking" TRBV17$^+$ TCRs from the naïve mouse CD8$^+$ T cell repertoire that recognize the H-2D^b–NP$_{366}$ epitope, we demonstrate that their inability to support T cell activation and in vivo recruitment is a direct consequence of reversed docking polarity and not TCR–pMHCI binding or clustering characteristics. Canonical TCR–pMHCI docking optimally localizes CD8/Lck to the CD3 complex, which is prevented by reversed TCR–pMHCI polarity. The requirement for canonical docking was circumvented by dissociating Lck from CD8. Thus, the consensus TCR–pMHC docking topology is mandated by T cell signaling constraints.

One-Sentence Summary: The highly conserved nature of T cell antigen receptor recognition is essential for colocalization of key signaling molecules

T cell–mediated immunity to pathogens and cancers requires activation of T cells through αβ T cell antigen receptor (TCR) recognition of antigenic peptides presented by MHC class I (MHCI) or class II (MHCII) molecules. The extreme diversity inherent in both the TCR repertoire and the array of pMHC ligands is reflected in the substantial variation at the TCR–pMHC interface (*1*). Despite this variation, nearly all of the TCR–pMHC ternary complexes solved to date exhibit a highly consistent docking polarity, with the TCRα chain sitting over the MHCI α2 or MHCII β1 helix, and TCRβ docking over the MHCI and MHCII α1 helix (*1*). Evidence suggests that the conserved TCR–pMHC docking polarity is "hard wired" by evolutionarily conserved amino acid motifs in the germline encoded regions of TCRs and MHC molecules (*2*–*5*). An alternate model suggests that TCR recognition of pMHC is driven during thymic selection by the need for the CD4 or CD8 coreceptors to bind MHC and deliver coreceptor-associated Lck to the CD3 signaling complex (*5*). Because of the proposed positioning of CD3 in the TCR–pMHC–CD4/CD8 complex, this model posits that only canonical polarity TCR–pMHC interactions are conducive to signaling (*6*–*8*). The biological significance of the canonical docking polarity remains unclear and has not been tested experimentally owing to the rarity of TCR–pMHC docking polarities outside of this paradigm (*1*, *9*–*11*). We recently identified $CD8^+$ T cells expressing "reversed" TCRs that bind their cognate pMHCI in a 180° reversed orientation, signaled poorly, and drove a weak antiviral immune response (*12*). Here, we investigated the key drivers of the canonical TCR–pMHC docking polarity and its role in T cell recognition and activation.

Results

Unconventional TRBV17$^+$ TCRs are prevalent in the naïve H-2D^b–NP$_{366}$-specific repertoire but do not contribute to the immune response

We have previously described two naïve TRBV17$^+$ TCRs (NP1-B17, hereafter referred to as B17.R1, and NP2-B17) that recognize the H-2D^b–NP$_{366}$ epitope in a 180° reversed orientation (*12*). To determine whether reversed TCR docking was a general feature of TRBV17$^+$ H-2D^b–NP$_{366}$-specific TCRs, we generated H-2D^b–NP$_{366}$ tetramers containing single amino acid substitutions at H-2D^b Glu18 and/or Ala89—residues that are uniquely important for binding the reversed B17.R1 TCRα chain (*1*, *12*). Ala89Glu substitution (H-2D^b–NP$_{366}$^{A89E}) completely abrogated tetramer binding to B17.R1 at high TCR expression levels without affecting B13.C1 TCR binding (**Fig. 1, A and B**). The loss of B17.R1 TCR binding was verified by surface plasmon resonance (SPR) analysis (**Fig. 1C** and **Table 1**).

We next used comparative staining with the H-2D^b–NP$_{366}$^{WT} and H-2D^b–NP$_{366}$^{A89E} tetramers to determine the proportion of the naïve H-2D^b–NP$_{366}$-specific CD8$^+$ T cell population that was impacted by this mutation, suggestive of a reversed TCR–pMHCI docking polarity (**Fig. 1, D and E**). Although a similar number of TRBV13$^+$ cells were detected using either tetramer (**Fig. 1F**), the mutant A89E tetramer detected only ~48% of TRBV17$^+$ cells detected by the WT tetramer (**Fig. 1G**). In contrast, these two tetramers showed equivalent stainin of both TRBV13$^+$ and TRBV17$^+$ T cells in mice infected with influenza A virus (IAV) (**Fig. 1, H to K**). Thus, although TRBV17$^+$ TCRs that bind H-2D^b–NP$_{366}$ in a reversed orientation are prevalent in the naïve repertoire, they are not recruited into the immune response after IAV infection.

Recruitment into the immune response is associated with TCR–pMHCI docking topology independently of TCR–pMHCI affinity

To gain a further understanding of TCR–intrinsic determinants of recruitment, we analyzed TRBV17^{+} H-2D^{b}–NP$_{366}$-specific TCRαβ sequences from uninfected (*13*) and infected B6 mice. The naïve TRBV17^{+} TCRαβ repertoire was diverse, comprising a range of TRAV genes with distinct CDR3α and CDR3β sequences (**Fig. 2A**) (*13*). By contrast, each immune repertoire was characterized by the dominance of only one or two clones (**Fig. 2B**). Thus, the low prevalence of TRBV17^{+} TCRs in the H-2D^{b}–NP$_{366}$-specific immune repertoire (*13*) is due to an inability of most of these clones to respond to IAV.

To demonstrate that the key criteria for immune recruitment from the TRBV17 subset was a canonical docking polarity, we selected three TRBV17^{+} TCRs from the immune repertoire for further structural and biophysical analyses. These TCRs were taken from expanded clones (mouse 1: B17.C1; mouse 3: B17.C2) and from the single TRAV14^{+} clone from mouse 3 (B17.R2) (**Fig. 2B**). Importantly, although the B17.R2 TCR was identified from an infected mouse, the sensitive detection method and apparent lack of clonal expansion means it was likely derived from a naïve T cell. We performed tetramer staining of 293T cells expressing these TCRs, along with a TRBV13^{+} TCR (B13.C1) known to drive robust immune recruitment (*12*, *13*). Those TCRs that were well represented in the immune response, including B13.C1 (**Fig. 2C**), B17.C1 (**Fig. 2D**), and B17.C2 (**Fig. 2F**), all showed equivalent binding by the H-2D^{b}–NP$_{366}^{WT}$ and H-2D^{b}–NP$_{366}^{A89E}$ tetramers. By contrast, the poorly represented or unrecruited B17.R2 TCR showed significantly reduced binding of the H-2D^{b}–NP$_{366}^{A89E}$ tetramer (**Fig. 2E**), and a 10-fold reduced affinity, suggesting a reversed TCR–pMHCI docking.

To determine the role of TCR–pMHCI affinity in driving immune recruitment of TRBV17^{+} cells, we determined TCR affinity by SPR (**Table 1**). The canonical immune B17.C1 TCR had an extremely weak affinity for H-2D^{b}–NP$_{366}$ (K_D>200 μM) (**Fig. 2D**). By contrast, the minor or naïve B17.R2 TCR had a substantially higher affinity (K_D=6.34 μM) and tetramer binding

(**Fig. 2E**), similar to that of the immunodominant B13.C1 TCR (K_D=4.13 μM) (**Fig. 2C**). Thus, the prevalence of T cells in the immune response is primarily associated with canonical TCR–pMHC docking polarity, independent of TCR–pMHC affinity.

Structural determination of TCR–H-2D^b–NP$_{366}$ docking topologies

We next determined the crystal structures of B17.R2 and B17.C1 TCRs in complex with H-2D^b–NP$_{366}$ (**Fig. 3**, tables S1 to S4). As suggested from tetramer binding (**Fig. 2**), the B17.R2 TCR adopted a reversed docking polarity over H-2D^b–NP$_{366}$, forming a docking angle of 238° and binding in a similar manner to the previously determined B17.R1–H-2D^b–NP$_{366}$ and NP2-B17–H-2D^b–NP$_{366}$ complexes (**Fig. 3, A and B,** and table S4) (*12*). By contrast, the B17.C1 TCR adopted a canonical docking polarity (**Fig. 3, C and D,** and table S4). In the B17.R2 TCR–H-2D^b–NP$_{366}$ complex, the TCRα chain played a lesser role (26.4% of BSA) in the interaction with only the CDR3α loop contributing to binding (**Fig. 3B** and table S4). By contrast, the TCRβ chain contributed to 73.6% of the BSA, encompassing the framework region of the β-chain (FWβ) region (39.2% BSA), the CDR2β loop (27.3% BSA), and the CDR3β loop (7.1 % BSA) (**Fig. 3B** and table S4). Similarly, the B17.C1 TCR–H-2D^b–NP$_{366}$ complex exhibited an unusually high contribution of the TCRβ chain (75% of BSA) with the interactions dominated by the CDR3β loop (37.8% of BSA) and the CDR2β loop (23.2% of BSA) (**Fig. 3D** and table S4). Moreover, this complex structure presents an unusually low number of contacts between the TCR and the MHCI (table S2), as well as a poor shape complementarity (table S4) and was consistent with the low affinity of this interaction (**Table 1** and table S2).

CD8$^+$ T cell recruitment does not correspond to 2D TCR–pMHCI affinities nor bond duration under force

To test the possibility that T cell recruitment correlated with 2D TCR–H-2D^b–NP$_{366}$ affinities, we measured the relative 2D affinity of B13.C1, B17.R1, B17.R2, and B17.C1 TCRs for H-

2D^{b}–NP$_{366}$ using the 2D micropipette adhesion frequency assay (2D–MP) (*14–18*). Although the reversed B17.R2 TCR had the second highest 2D affinity after the B13.C1 TCR (fig. S1A), it was not conducive to robust immune recruitment **(Fig. 2B)**. By contrast, the canonical docking B17.C1 TCR with a lower 2D affinity (fig. S1A) was expanded in the immune repertoire (**Fig. 2B). **Thus, the recruitment of the H-2D^{b}–NP$_{366}$-specific TRBV17^{+} T cells occurs independently of TCR–pMHCI affinity.

We next measured the TCR–H-2D^{b}–NP$_{366}$ bond lifetime under conditions of force (*14–17*). CD8^{+} TCR transductants were stimulated with peptide bound to H-2D^{bWT} or to mutant H-2D^{bD227K} to assess the contribution of coreceptor binding to bond strength (*19*). Both of the canonical docking TCRs—the high-affinity B13.C1 TCR and low-affinity B17.C1 TCR—were able to form catch bonds, peaking at around 10 pN (fig. S1, B and C). CD8 binding contributed significantly to bond lifetime only for the low-affinity B17.C1 TCR (fig. S1, B and C). By contrast, reversed polarity TCRs (B17.R1 and B17.R2) showed the formation of slip bonds with pMHCI, with a loss of bond lifetime with increasing force (fig. S1, D and E**)**. Intriguingly, however, at least for the high-affinity B17.R2 TCR, the bond lifetime generated at ~10 pN—an approximation of the physiological force on a TCR (*20–22*)—was similar to that observed at the peak of the catch bond formation (fig. S1F). Thus, although the reversed TCR–H-2D^{b}–NP$_{366}$ interaction is characterized by slip-bond formation, it exhibits relatively high bond lifetimes at the physiological force of 10 pN.

Only canonical docking TCRs can support immune recruitment, irrespective of TCR–H-2D^{b}–NP$_{366}$ affinity

To confirm our earlier observations (**Fig. 1, D to K**) that T cell recruitment into the immune response was primarily dependent on a canonical TCR–pMHCI docking polarity independent of TCR–pMHCI binding strength, we selected B17.R1, which binds with low-to-moderate affinity, and the B17.R2 TCR, which binds with high-affinity similar to that of the immunodominant B13.C1 TCR, for further investigation. We then generated retrogenic mice expressing the canonical polarity B13.C1 or B17.C2 TCRs, and the reversed polarity B17.R1 or B17.R2 TCRs (*23*). We were unsuccessful in expressing the B17.C1 TCR in vivo despite validating construct fidelity and instead generated TCR retrogenic mice expressing the B17.C2 TCR, which exhibited similar properties. Namely, it expressed TRBV17, had a moderate to low avidity for H-2D^b–NP$_{366}$, bound H-2D^b–NP$_{366}$ independently of Ala89 (and thus likely docked in a canonical orientation) (**Fig. 2F**), and was expanded in the immune repertoire (**Table 1**). Consistent with our previously published data (*12*), adoptive transfer of retrogenic B13.C1$^+$ and B17.R1$^+$ T cells, either alone or in combination, followed by IAV challenge (**Fig. 4A**), resulted in the effective recruitment and expansion of canonical B13.C1$^+$ T cells but not reversed B17.R1$^+$ T cells (**Fig. 4, B to N,** and fig. S2A). Failure to recruit B17.R1$^+$ T cells was not due to GFP expression since the same experiment performed with GFP$^+$ B13.C1$^+$ T cells showed similar recruitment profiles as those coexpressing mCherry (fig. S2, B to E).

To distinguish the impact of TCR–pMHCI affinity and docking polarity on recruitment, we adoptively transferred T cells expressing the high-affinity reversed B17.R2 TCR, either alone or with B13.C1$^+$ T cells prior to IAV challenge. The B17.R2 T cells were not detectable in the immune response after either single (**Fig. 4, C to E**) or cotransfers (**Fig. 4, B, I to K**). Finally, we adoptively transferred the low-to-moderate-avidity, canonical B17.C2$^+$ T cells and the high-affinity, reversed B17.R2$^+$ T cells into B6 mice, which were then challenged with IAV. Retrogenic B17.C2$^+$ T cells were readily recovered from bronchoalveolar lavage (BAL) (**Fig. 4, B, C and L**), spleen (**Fig. 4, D and M**), and mLN (**Fig. 4, E and N**). By contrast, the B17.R2 TCR did not support detectable immune expansion into any tissue (**Fig. 4, L to N**). Thus, TCR–pMHCI docking topology supersedes TCR–pMHCI affinity as the primary determinant for effective in vivo immune recruitment.

Reversed polarity TCRs do not prevent TCR clustering

To determine whether the reversed TCR–pMHCI docking prevents the formation of signaling competent multimers (*10*), 5KC T cell hybridoma cells (TCRαβ$^-$CD4$^-$CD8$^-$) (*24*) expressing either the B13.C1 or B17.R2 TCRs were placed on a supported lipid bilayer (SLB) containing ICAM-1 (unstimulated) or ICAM-1 and H-2D^b–NP$_{366}$ (stimulated) (**Fig. 5, A and B**) for analysis of TCR clustering by *d*STORM (**Fig. 5A**). For both unstimulated and stimulated T cells, TCRs exhibited a non-random clustered spatial distribution on the cell membrane, as indicated by a significantly larger L(*r*)-*r* value relative to complete spatial randomness (**Fig. 5B**). The peak of molecular TCR clustering (Max L(*r*)-*r*), was higher following stimulation (ICAM+pMHCI) compared to unstimulated T cells (ICAM), indicative of antigen-driven TCR clustering (**Fig. 5, B and C**). This antigen driven TCR clustering was similar for both the canonical (B13.C1) and reversed (B17.R2) docking TCRs. Thus, reversed TCR–pMHCI docking does not impede the formation of multimeric TCR–CD3 structures.

Reversed TCR recognition of H-2D^b–NP$_{366}$ impedes the localization of CD3 and CD8

Assuming that a similar arch-like structure is formed following pMHCI recognition by the TCR/CD3 and CD8 as has been observed for TCR–pMHCII–CD4 (*25*), the canonical TCR–pMHC docking polarity may be essential for coreceptor–associated Lck to be situated proximally to CD3 for the initiation of signal transduction (*25*). Using our current structural understanding of the interactions between TCR–pMHCI (*1*), MHCI and CD8 (*26*) and TCRαβ and the CD3 chains (*27*, *28*), we modeled the quaternary TCR–pMHC–CD8–CD3 structure for canonical-polarity B17.C1 TCR–H-2D^b–NP$_{366}$ (**Fig. 5D**) and reversed-docking B17.R1 TCR–H-2D^b–NP$_{366}$ interactions (**Fig. 5E**). The 180° reversal of the B17.R1 TCR over the H-2D^b–NP$_{366}$ dramatically altered the position of CD8 relative to CD3.

To experimentally determine whether reversed TCR–pMHCI docking impacted the localization of CD8–associated Lck to the CD3 complex, we used FLIM–FRET microscopy to determine close (<10 nm) molecular association between CD8β–mCherry and CD3ζ-GFP fusion proteins in live TCR$^+$ hybridoma cells after epitope-specific stimulation (*29–32*) as this was not readily feasible in primary T cells. We used the FLIM–FRET approach over conventional super-resolution microscopy (20–30-nm resolution) to allow us to resolve protein–protein interactions (<10 nm). Expression of the FRET pair constructs (fig. S3A) did not negatively affect TCR signaling since pERK could be detected after stimulation of the B13.C1 TCR$^+$ 5KC$^{\mathrm{CD3}\zeta\mathrm{GFP.CD8}\alpha\beta\mathrm{mCherry}}$ cells, similar to B13.C1 TCR$^+$ 5KC T cells expressing WT CD8αβ and CD3ζ (**Fig. 6F** and fig. S3, B to D). Stimulation of B13.C1 TCR$^+$ cells resulted in FRET, as measured by a substantial reduction in the amplitude weighted lifetime of the donor (GFP) at the synapse (fig. S3E and S3F), indicating colocalization of the CD8β^{mCherry} and CD3ζ^{GFP} molecules (**Fig. 5, F and G**). We also observed FRET after stimulation of cells expressing the canonical B17.C1 and B17.C2 TCRs (**Fig. 5, F and G**). However, stimulation of cells expressing the reversed B17.R1 and B17.R2 TCRs resulted in negligible FRET (**Fig. 5, F and G**). Thus, a reversed TCR–pMHCI docking topology results in improper localization of CD8β^{mCherry} and CD3ζ^{GFP} in a manner that is independent of the strength of TCR–pMHCI binding.

The CD8 coreceptor inhibits TCR signaling by reversed-polarity TCRs

We hypothesized that when TCR–pMHCI polarity is reversed, the association of Lck with CD8 prevents, rather than promotes, effective Lck localization to CD3. To test this, 5KC T cells were transduced with either the high-affinity canonical B13.C1 TCR or the high-affinity reversed B17.R2 TCR (**Fig. 6, A to C**) as neither of these TCRs are dependent on CD8 for binding to H-2D^b–NP$_{366}$ (fig. S1, B, E and F). Each TCR was expressed (1) with WT CD8αβ (CD8$^{\mathrm{WT}}$) (**Fig. 6A**); (2) in the absence of CD8 (CD8$^{\mathrm{NULL}}$) (**Fig. 6B**); or (3) with mutant CD8αβ containing C227A and C229A substitutions in the cytoplasmic tail of CD8α to abrogate Lck binding (CD8$^{\mathrm{CxC}}$) (*33*) (**Fig. 6, C to E**). All cell lines showed a similar sensitivity to PMA–

ionomycin stimulation or antibody-mediated polyclonal stimulation, as measured by pERK or IL-2 production (fig. S4).

The CD8^{WT} B13.C1 TCR^{+} transductants mediated robust signaling throughout the time-course, inducing a significantly higher pERK signal magnitude and IL-2 secretion compared to B17.R2 (**Fig. 6F**). For B13.C1 pERK was induced as early as 10 min and maintained for 60 min after stimulation, and substantial IL-2 production at 16 hours (**Fig. 6F**). By contrast, the high-affinity reversed B17.R2 TCR showed negligible signal transduction when coexpressed with CD8^{WT}, as evidenced by minimal pERK and no detectable IL-2 (**Fig. 6F**). Intriguingly, while the loss of CD8 (CD8^{NULL}) severely attenuated the signal transduction capacity of the B13.C1 TCR, detectable, low-level pERK and IL-2 secretion was evident following stimulation of B17.R2 TCR^{+} cells (**Fig. 6G**) and was statistically indistinguishable from B13.C1. To distinguish the contribution of CD8 to MHCI binding versus Lck delivery, we stimulated cells expressing the mutant CD8^{CxC}. Again, both the B13.C1 TCR^{+} and B17.R2 TCR^{+} cells transduced a signal of similar kinetics and magnitude, with increased pERK than was observed in the absence of CD8 (**Fig. 6H**). This signaling again corresponded to detectable and equivalent levels of IL-2 production. Similar findings were made upon analysis of 5KC$^{\zeta GFP.CD8\beta mcherry}$ T cells (fig S3B-D) and independently generated B13.C1, B17.R1 and B17.R2 TCR^{+} cells (fig. S5A). These findings were also in agreement with TCRβ downregulation analysis after stimulation (fig. S5B).

Thus, signaling mediated by canonical TCR–pMHCI docking is augmented slightly by CD8 binding and substantially by CD8 delivery of Lck. However, reversed polarity TCR–pMHCI recognition prevents signaling due to CD8 sequestration and mislocalization of Lck. We present evidence that the highly conserved TCR–pMHCI docking polarity is mandated not by binding requirements, but instead by the need to colocalize key signaling molecules to enable signal transduction.

Discussion

Although a topic of much speculation, there has been no definitive demonstration of whether the canonical TCR–pMHC docking polarity potentiates effective TCR binding or signaling, nor the mechanism by which it does so. Although evolutionarily conserved pairwise interactions between TCR and MHC molecules can predispose TCRs to MHC recognition in a canonical orientation (*5*), our data revealed that the inability of reversed TCR–pMHC recognition to support T cell activation was unrelated to binding affinity. Instead, these findings support a paradigm in which the polarity of TCR recognition of pMHCI is a primary determinant of T cell signaling, via the colocalization of molecules critical for TCR signal transduction.

Our data aligns with current knowledge of the structural organization of TCR signaling molecules. The complete ternary structure of a TCR–pMHCII–CD4 complex (*25*) revealed the formation of a 70-Å wide "arch" between the TCR and the CD4 coreceptor, within which the asymmetrically arranged CD3 signaling complex (*28*) is positioned. It was postulated that extreme docking polarities (such as a reversed polarity) would place the bulk of the CD3 complex outside of the arch, impeding optimal Lck delivery (*25*) and T cell signaling.

Our current work provides clear support for this model by demonstrating that the inability of reversed TCRs to signal (1) occurs independently of binding strength; (2) is dependent on CD8 binding of Lck; and (3) is characterized by an inability to colocalize CD8 and CD3 after antigen stimulation. Moreover, our demonstration of robust TCR–CD3 cluster formation suggest that unusual docking topologies do not preclude signaling by inhibiting TCR multimerization (*10*, *34*), in line with previous work showing that dense TCR–CD3 cluster formation can occur independently of signaling, and better reflects TCR binding (*35*). Our observation that the reversed TCR–pMHCI interaction formed slip bonds and yet remains inherently capable of signal transduction, supports the notion that catch bonds are not essential (although likely still optimal) for signaling.

The observation that CD8 was an impediment to signaling by reversed TCR–pMHCI recognition, via binding of Lck, demonstrated that this polarity resulted in a mislocalization of coreceptor-associated Lck and CD3 following pMHCI ligation. Previous studies have shown that preventing coreceptor sequestration of Lck in vivo either by deletion of coreceptors (*36*) or mutation of coreceptor binding sites on Lck (*37*), facilitates TCR signaling following recognition of non-MHC ligands. Thus, the association of Lck with the CD8 coreceptor, in addition to dictating the MHC ligand (*5*), also dictates the manner in which the MHC ligand must be recognized.

Other deviations from the typical TCR–pMHC docking angle exist. Most notably, two identified human induced regulatory T cell (iTreg) TCRs were found to dock on pMHCII in a reversed orientation (*9*). Although broadly maintaining the canonical docking polarity, extreme docking angles over the pMHC have been observed in autoreactive human CD4$^+$ T cells (*38*, *39*), and in a non-signaling mouse H-2L^d-restricted TCR (*10*). The current study provides a potential mechanism by which such unconventional pMHC docking polarities may diminish TCR signaling to prevent negative selection or abrogate TCR-mediated signaling. Such exceptions to the canonical TCR–pMHC docking "rule" should be explored to further advance our understanding of T cell signaling requirements.

Although Lck association with coreceptors can have a dramatic effect on TCR signaling, some intracellular Lck untethered to coreceptors is present, highly active (*40*, *41*), and able to support in vivo signaling (*30*, *36*, *37*). Why then, does "free" Lck not allow for signaling by reversed TCRs? Critically, Lck can be found associated with the TCR–CD3 complex in mice lacking CD4 and CD8 coreceptors but not in mice expressing coreceptors (*36*). We propose that when coreceptors are expressed, Lck is preferentially sequestered away from the TCR–CD3 complex to impair TCR signaling in the absence of MHC ligands. In the presence of MHC ligands, the coreceptor delivers Lck and promotes MHC-restricted TCR signaling. This may be exacerbated in the case of CD4, which binds Lck with higher affinity than CD8 (*42*, *43*). Although small amounts of residual free Lck may be able to initiate some early phosphorylation events (*32*), it is insufficient to support full activation.

Although a useful tool for dissecting out the mechanism constraining signaling-competent modalities of TCR recognition, the drivers of reversed TCR docking in this instance are unclear. It has been suggested that a reversed TCR–pMHC orientation may be a consequence of positively charged residues and/or proline within the CDR3β loop, preventing interaction with a conserved cluster of positively charged residues on the CDR3β contact regions of MHCI α2 helices (*44*). A comparison of the CDR3β loops of naive TRBV17^{+} (enriched for reversed TCRs) and immune H-2D^{b}–NP$_{366}$-specific repertoires (*13*) (enriched for canonical TCRs) revealed a similar frequency of His, Lys, Arg, and Pro usage. However, given the TRBV17 gene element encodes an Arg at position 108, all but one of the naïve TRBV17^{+} TCRs contained at least one of these residues while they were present in only around 40% of the immune CDR3β sequences. Thus, the relevance of these residues in driving non-canonical docking requires further investigation.

The inability of the reversed TCRs to support signaling would appear to preclude their ability to support thymic selection. It is possible, given the reduced threshold for thymic selection compared to peripheral activation (*45–48*) that an attenuated signal may be sufficient for positive selection. Alternatively, such TCRs may mediate selection via canonical TCR–pMHC recognition and exhibit unconventional pMHC recognition only in the periphery.

In summary, the current study demonstrates a dual role for coreceptor association of Lck; augmenting signaling mediated by canonical TCR–pMHC interactions and preventing signaling by unconventional modes of recognition. We hypothesize that in this way excessive

TCR cross–reactivity is constrained by the number of signaling competent binding modalities, thereby enhancing the exquisite functional specificity of the TCR–pMHC interaction.

Materials and Methods

TCR transfection of HEK293T cells

HEK293T cells (ATCC, #CRL-3216) were maintained in a humidified incubator at 37°C and 10% CO_2. HEK293T cells were plated 3.5×10^5 cells/well of a six-well plate in a 3.5 ml of complete medium (DMEM (Gibco 11960), 10% FCS, HEPES, L-glut, PenStrep). The following day, 4.2 µl of FuGene 6 HD (Promega) was added to 171 µl of OptiMEM (Gibco) in an Eppendorf tube and incubated for 10 min at RT. The FuGene:OptiMEM mixture was then added dropwise to 700 ng of pMIGII encoding an αβTCR sequence and 700 ng of pMIGII encoding CD3γδε and ζ subunits and incubated for a further 15 min at RT. The FuGene-OptiMEM-DNA mixture was then added dropwise to each well of a six-well plate and swirled to mix gently before returning to the incubator. After 48 hours, culture medium was aspirated and cells were detached from the plate by repeated washing with FACS buffer (PBS + 0.1% BSA). Transfected cells were labeled with indicated tetramers for 1 hour at RT followed by staining for TCRβ and viability. Tetramer binding was analyzed by flow cytometry using a Fortessa X20 (BD Biosciences).

Mice and influenza A virus infection

Female C57BL/6J (CD45.2) mice were bred and housed at the Monash Animal Research Platform (MARP; Monash University, Victoria, Australia). B6.SJ^{ptprca} (CD45.1) and *Rag1*$^{-/-}$ (CD45.2) mice were purchased from the Walter and Eliza Hall Institute and housed at MARP. Naïve Female C57BL/6J mice aged 6–10 weeks were briefly anesthetized by isoflurane inhalation and infected intranasally with 1×10^4 PFU HKx31 (H3N2) influenza A virus in 30 µl of saline. All animal experimentation was reviewed and approved by the Monash University Animal Ethics Committee (AEC8585, AEC14182 and AEC17693).

Tetramer-based magnetic enrichment for H-2D^b–NP$_{366}$-specific T cells

Tetramer-based magnetic enrichment of epitope-specific T cells was performed largely as described (*49*, *50*). Spleens and all easily dissected lymph nodes were harvested from 10 naïve female C57BL/6J mice (pre-immune repertoire) or individual mice 10 days post infection with HKx31 IAV i.n (immune repertoire). One female C57BL/6J mouse infected with HKx31 between 10–60 days post infection was also harvested to be used as a positive control for tetramer staining of naïve samples. For analysis of the pre-immune repertoire, single-cell suspensions from 10 naive mice were pooled and then evenly divided into eight separate 50-ml conical centrifuge tubes, each for enrichment through an LS column (Miltenyi Biotec). For analysis of immune repertoires samples from individual mice were split evenly into two matched 50-ml conical centrifuge tubes. Each experimental sample was first blocked using Fc block (2.4G2 supernatant + 1% normal mouse serum + 1% normal rat serum). Each pair of tubes were labeled with either H-2D^{bWT}–NP$_{366}$ or H-2D^{bA89E}–NP$_{366}$ tetramers conjugated to APC for 1 hour at RT. Tetramer-labeled cells were then incubated with anti-APC microbeads (Miltenyi Biotec) for 30 min at 4°C. Tetramer-bound cells were positively enriched by passage through an LS column (Miltenyi Biotec) mounted on a QuadroMACS (Miltenyi Biotec) magnetic separator. Enriched samples were then labeled with antibodies (as listed in table S5) against cell-surface antigens; including Vβ9 (TRBV17) and Vβ8.3 (TRBV13-1) and stained for viability before analyzing entire samples on a Fortessa X20 (BD Biosciences) or Symphony A3 (BD Biosciences) flow cytometer.

Single-cell TCR sequencing and T cell cloning of immune TRBV17^{+} H-2D^{b}–NP$_{366}$–specific T cells

Tetramer-bound cells were enriched and isolated as described above for immune repertoires. Samples enriched for tetramer bound cells were run on a FACSAria III (BD Biosciences) cell sorter and live CD19^{-}CD4^{-}CD8^{+}TCRβ^{+}CD44^{+}Vβ9^{+} H-2D^{b}–NP$_{366}$-specific T cells were single-cell-sorted using a FACS AriaIII Fusion (BD Biosciences) into 96-well PCR plates

(Eppendorf) and stored at −80°C until use. Single-cell multiplex RT-PCR of αβTCR was performed as previously described (*13*). PCR product was sequenced by Sanger sequencing at the Monash Micromon Genomics Facility (Monash University, VIC, Australia). Antigen-specific P2A linked TCRαβ gene constructs were custom ordered from Genscript and cloned into pMIGII (RRID: Addgene_52107; a gift from D.A.A. Vignali) vector and sequenced to confirm the correct TCR sequence. Plasmids encoding antigen specific P2A linked TCRαβ were prepared and propagated for retroviral transduction using 10-beta Competent *Escherichia Coli* (*E. coli*) (New England Biolabs CR019H) and plasmids were isolated using the EndoFree Maxi Prep Kit (Qiagen 12362).

Generation of TCR retrogenic mice

Plasmids encoding TCRα and TCRβ genes of interest linked by P2A peptide were ordered from Genscript and cloned into the pMIGII or pMIC vector expressing GFP or mCherry, respectively (RRID: Addgene_52107, RRID:Addgene_52114; a gift from D.A.A. Vignali). TCR retrogenic mice were generated as previously described (*12*, *23*) but with the use of congenically distinct female *Rag1*$^{-/-}$ (CD45.2) mice as bone marrow donors and female *B6.SJ*^{ptprca} (CD45.1) as recipients to aid the identification of donor-derived cells.

Adoptive transfer of retrogenic CD8$^+$ T cells for IAV challenge

CD45.1$^-$CD45.2$^+$CD4$^-$CD8$^+$ GFP/mCherry$^+$ T cells were isolated by FACS from female TCR retrogenic mice using a BD FACSAria III Fusion or BD Influx cell sorter (BD Biosciences). Retrogenic T cells (4×10^3) from each line were resuspended in 200 µl of PBS + 2% FCS and injected intravenously into naïve female *B6.SJ*^{ptprca} (CD45.1) mice. The next day, mice were infected with 1×10^4 PFU HKx31 IAV as described. At the peak of the CD8 T cell response (10 days post infection), mice were euthanized and bronchoalveolar lavage (BAL), spleen, and mediastinal lymph nodes (mLN) were harvested for flow cytometry analysis. Gating strategy for identifying donor derived retrogenic T cells can be found in fig. S3.

In vitro TCR expression by retroviral transduction

TCR^{null} 5KC cells (TCRαβ$^-$CD4$^-$CD8$^-$) (gift from P. Marrack) were maintained in a humidified incubator at 37°C and 10% CO_2. 5KC cells were sorted for loss of CD4 to establish a CD4$^-$CD8$^-$TCR$^-$ cell line. HEK293T cells were plated 1×10^6 cells/dish in a 15-cm tissue culture dish (Sarstedt) in 10 ml of complete medium (cDMEM; DMEM, 10% FCS, HEPES, L-glut, PenStrep). The following day, 30 µl of FuGene 6 HD (Promega E2691) was added to 470 µl of OptiMEM (Gibco 31985) in a microcentrifuge tube and incubated for 10 min at RT. The FuGene:OptiMEM mixture was then added dropwise to 4 µg of pMIGII encoding an αβTCR sequence and 4 µg of pPAM-E and 2 µg of pVSVg and incubated for a further 15 min at RT. The FuGene-OptiMEM-DNA mixture was then added dropwise to the HEK293T cell culture and swirled to mix gently before returning to the incubator. The next day, medium containing FuGene:OptiMEM:DNA was replaced with fresh cDMEM and incubated for 12 hours. Supernatant was removed approximately every 12 hours five to six times and filtered through a 0.45-µm syringe driven filter. Polybrene (Sigma H9268) (6 µg/ml) was added to the supernatant before resuspending 5KC cells in filtered retrovirus containing supernatant. After five to six virus transfers, 5KC cells were grown to confluency in fresh cDMEM and sorted for similar TCRαβ and CD8αβ expression. For CD8 transductions, only cells expressing an endogenous ratio of CD8α:CD8β were sorted.

pERK detection by phospho-flow cytometry

For a positive control, 96-well U-bottom plates were coated overnight with 100 µl of anti-mouse CD3 antibody diluted to 10 µg/ml in PBS overnight. DC2.4 cells (gift from K. Rock) were cultured in cDMEM and maintained in a humidified incubator at 37°C and 10% CO_2. DC2.4 cells were stained with Aqua Blue Fixable viability stain (Life Technologies) and seeded at 1×10^5 cells/well in 50 µl of a 96-well plate (Nunc) and allowed to adhere for 1 hour in the incubator. Transduced 5KC cell lines were labeled with Aqua Blue Fixable viability stain

(Life Technologies) and plated at 50,000 cells/well and allowed to equilibrate in the incubator for at 1 hour. NP_{366} peptide (Genscript) was then added to the DC2.4 cultures at indicated concentrations and incubated for a further 1 hour. 5KC cells (5×10^4) were added to peptide-pulsed DC2.4 cultures at a final culture volume of 100 µl and briefly centrifuged at 600*g* for 1 min to encourage contact. At the indicated time points, 100 µl of pre-warmed 2X Lyse/Fix buffer (BD Biosciences 558049) was added to each well and incubated at 37°C for 10 min. Fixed cells were washed twice in 200 µl of PBS. Fixed cell pellets were permeabilized by addition of 100 µl of −20°C Perm Buffer III (BD Biosciences) and then stored overnight at −20°C. The following day fixed and permeabilized cells were washed with 200 µl of FACS buffer and stained with cell surface antibodies and a rabbit anti-phospho p44 MAPK (Cell Signaling Technology) for 1 hour on ice. Cells were washed with FACS buffer and then stained with an anti-rabbit PE $F(ab')_2$ fragment (Cell Signaling Technology) for 30 min. Cells were washed twice in FACS buffer before running the samples on a BD Fortessa X20 or BD Symphony A3 (BD Biosciences) flow cytometer.

IL-2 ELISA

DC2.4 cells were seeded at 1×10^5 cells/well in 100 µl of a flat-bottom 96-well plate (Nunc) and allowed to adhere for 1 hour in the incubator. Transduced 5KC cell lines were plated at a concentration of 1×10^6 cells/ml and allowed to equilibrate in the incubator for at least 1 hour. NP_{366} peptide was then added to the DC2.4 cultures at indicated concentrations and incubated for a further 1 hour. 5KC cells (5×10^4) were added to peptide pulsed DC2.4 cultures or to the anti-CD3 coated wells at a final culture volume of 200 µl and briefly centrifuged at 600*g* for 1 min to encourage contact. After 16 hours of coincubation, plates were centrifuged at 935*g* for 3 min to pellet cells and supernatant was aspirated and transferred to a new plate and stored at −20°C until required. IL-2 secreted in the supernatant was measured using the BD IL-2 mouse

ELISA kit (BD Biosciences 555148) according to the manufacturer's instructions. Absorbance was measured at 450 nm using a CLARIOstar plate reader (BMG LabTech).

Immunoprecipitation and immunoblotting

5KC T cells (1.5-2×10^7) were lysed for 60 min at 4°C in 300 µl of Pierce® IP Lysis/Wash Buffer (25 mM Tris-HCl pH 7.4, 150 mM NaCl, 1% NP-40, 1 mM EDTA, and 5% glycerol) and 1X Halt™ Protease Inhibitor Cocktail (Pierce). Lysates were centrifuged at 13,000*g* for 20 min and 30 µl of supernatant was kept as whole-cell lysate/input. The remaining lysate was pre-cleared with 20 µl washed Protein G Sepharose for 60 min at 4°C. Protein G Sepharose (20 µl) was incubated with 10 µg of anti-CD8α (53-6.7) for 60 min at 4°C. Antibody-conjugated Protein G Sepharose was washed three times with Pierce® IP Lysis/Wash Buffer. Immunoprecipitation was performed by addition of pre-cleared lysate to antibody-conjugated Protein G Sepharose and incubation for 3 hours at 4°C. Samples were centrifuged, washed five times in Pierce® IP Lysis/Wash Buffer and once in 50 mM Tris-HCl (pH 7.4). Elution was performed by boiling in 3X Laemmli Buffer with 50 mM DTT (95°C, 5 min). Samples were centrifuged and supernatant containing immunoprecipitated CD8 was collected. Samples were resolved on 10 to 14% SDS-PAGE under reducing conditions at 100 V for 3-4 hours. Proteins were wet transferred onto PVDF membranes at constant 300 mA for 2 hours. Membranes were blocked for 60 min at RT in 5% skim milk (w/v) in 0.1% (v/v) TBS-Tween prior to incubation with specific antibody (1:3000) overnight at 4°C. Membranes were washed three times in 0.1% (v/v) TBS-Tween and probed with relevant horseradish peroxidase-conjugated secondary antibody as indicated for 60 min at RT. Following three washes in 0.1% (v/v) TBS-Tween, ECL substrate was added to membranes for 2 min. Blots were visualized on a ChemiDoc XRS+ (Bio-Rad Laboratories).

Confocal and fluorescence lifetime imaging (FLIM) for analysis of Förster resonance energy transfer (FRET)

DC2.4 cells were maintained in phenol free cDMEM (Gibco 31053). DC2.4 cells were seeded in 35-mm Fluorodish (World Precision Instruments) cell culture dishes at 1×10^5 cells/dish in 1 ml of culture and incubated overnight at 37°C and 10% CO_2. The following day, DC2.4 cells were washed three times with pre-warmed PBS and then stained with 5 µM CellTrace Violet (CTV; Invitrogen C34557) for 30 min. CTV was then aspirated from the dish and the labeled cells were washed three times with pre-warmed phenol free cDMEM. Labeled DC2.4 cells were incubated with 10 µM NP_{366} peptide for 1 hour. 5KC hybridoma cells expressing TCR and the FRET pairs CD3ζ-GFP and CD8β-mCherry were plated at a density of 1×10^6 cells/ml in a six-well dish and were equilibrated in the incubator for at least 1 hour before use. For imaging, DC2.4 cells were brought into focus and then 100 µl of T cells (approximately 1×10^5 cells) were added to the culture dish containing labeled DC2.4 cells and then imaged by confocal microscopy up to 20 min later using an Olympus FV1000 running Fluoview software (Olympus). Fluorescent lifetime of the donor molecule GFP was measured by time-correlated single photon counting (TCSPC) using a PicoHarp 300 (PicoQuant) running Symphotime 64 (PicoQuant) fitted to an Olympus FV1000 laser scanning confocal microscope. The laser set up was a 485-nm pulsed laser. TCSPC decay curves were fitted to a biexponential reconvolution decay model in SymphoTime 64 to determine donor (GFP) lifetime. A good biexponential reconvolution decay curve fit was characterized by χ^2 values close to 1. χ^2 values that deviated by ±1 were uncommon in our dataset but were excluded from the analysis. To detect FRET, the amplitude weighted donor average lifetime (τ_{AvAmp}) was used as this reflects the quenching of the donor due to the FRET process. To determine FRET between CD8β-mCherry and CD3ζ-GFP, we measured τ_{AvAmp} at the immunological synapse where the T cell interacted with a dendritic cell by selecting a region of interest (ROI) in the FLIM image. Non-synaptic τ_{AvAmp} was also measured from the same cell as an internal control and was used to calculate the percentage change in τ_{AvAmp} of GFP at the synapse (Syn$\Delta\tau_{AvAmp}$). For analysis, n-exponential reconvolution using n=2 model parameter was used for donor curve fitting.

2D micropipette adhesion frequency assay (2D-MP)

The relative 2D affinity of the H-2D^b restricted nucleoprotein epitope (NP$_{366}$; ASNENMETM) TCRs expressed in 5KC hybridoma cell lines was measured by the previously described 2D-MP (*14–18*). In short, human red blood cells (hRBCs) coated with Biotin-LC-NHS (BioVision) streptavidin (ThermoFisher Scientific) and then coated with biotinylated H-2D^b–NP$_{366}$^{D227K} and then mounted on a glass micropipette. 5KC hybridomas expressing either B13.C1, B17.R1, B17.R2 and B17.C1 TCRs were mounted on opposing glass micropipette. The adhesion frequency between the TCR of interest and pMHC aspirated on opposing micropipettes was observed using an inverted microscope. An electronically controlled piezoelectric actuator brought the opposing cells into contact and repeated a T cell contact and separation cycle with the pMHC coated RBCs 50 times while keeping contact area (Ac) and time (t) constant. Upon retraction of the T cell, adhesion (binding of TCR–pMHC) was observed as a distention of the RBC membrane, allowing for quantification of the adhesion frequency (Pa) at equilibrium. Surface pMHC (ml) and TCRb (mr) densities were determined by flow cytometry using an anti-TCRβ PE antibody (H57-597; BD Biosciences) and an anti-H2D^b antibody (clone:28-14-8; eBioscience) both at saturating concentrations along with BD QuantiBRITE PE beads for standardization (BD Biosciences). The calculation of molecules per area was determined by dividing the number of TCR and pMHC per cell by the respective surface areas. The relative 2D affinities were calculated using the following equation: AcKa=–ln[1–Pa(1)]/mrml.

Biomembrane force probe (BFP) assay

Bond-lifetime measurements under force were captured using the biomembrane force probe (BFP) assay. Procedures for coupling pMHC to glass beads have been described previously (*21*). Briefly, hRBCs were first biotinylated with EZ-link NHS-PEG-Biotin (Thermo Fisher

Scientific) and then reacted to streptavidin. Borosilicate beads were first cleaned, silanized, and then reacted to streptavidin–maleimide (Sigma-Aldrich, St. Louis, MO). Streptavidin beads were then coated with H-2D^b–NP$_{366}$ or H-2D^b–D227K-NP$_{366}$. pMHC monomer coated beads (which serve as a force probe) were then placed on the apex of a hRBC that was aspirated onto a glass micropipette. The position of the edge of the bead was tracked by a high-resolution camera (1,600 frames/s) with < 3-nm displacement precision. The position of the edge of the bead was tracked by a high-resolution camera (1,600 frames/s) with <3 nm displacement precision using a Zeiss microscope. The cell was brought into contact with the pMHC coated bead:RBC, the cell was then retracted and held at the desired force by the computer-controlled piezoelectric actuator until bond dissociation occurred. If adhesion was present, it was detected by tensile force caused by stretching of the hRBC and tracked by displacement of the pMHC coated bead. The bond lifetime was measured from the time the desired force was reached to the time it took the cell to disengage with the bead which was visualized as the RBC retracted and the bead returned to its starting position before the start of the next cycle. Repeated cycles (known as force-clamp cycles) could be performed. Multiple forces were collected for each ligand (pMHC coated beads) and were shown in 5-8 bins as the mean ± s.e.m. For an optimal response to antigen bond lifetimes increase with increasing force before reaching a peak and then decrease, which is referred to as a catch bond. When increasing force leads to decreasing bond lifetime this is termed a slip bond.

Supported Lipid Bilayer (SLB) preparation

Glass coverslips of a 0.17-mm thickness were first cleaned with 1M KOH for 10 min and then rinsed with MilliQ water and placed in 100% ethanol for 20 min. These glass coverslips were then plasma cleaned for 5 min. Afterwards, the coverslips were adhered to eight-well silicon chambers (ibidi, 80841). A liposome solution of 1 mg/ml with a lipid ratio of 96.5% DOPC (1,2-dioleoyl-sn-glycero-3-phosphocholine), 2% DGS-NTA(Ni) (1,2-dioleoyl-sn-glycero-3-

[(N-(5-amino-1-carboxypentyl)iminodiacetic acid)succinyl] (nickel salt)), 1% Biotinyl-Cap-PE (1,2-dioleoyl-sn-glycero-3-phosphoethanolamine-N-(cap biotinyl) (sodium salt)), and 0.5% PEG5000-PE (1,2-distearoyl-sn-glycero-3-phosphoethanolamine-N-[methoxy(polyethylene glycol)-5000] (ammonium salt) (mol%; all available from Avanti Polar Lipids (DOPC, 850375C), (DGS-NTA(Ni), 790404C), (Biotinyl-Cap-PE, 870273C), (PEG5000-PE, 880220C) was created by vesicle extrusion, as described previously (*35*). Extruded liposomes were added to eight-well chambers at a ratio of 1:5 with MilliQ water (with 10 mM of $CaCl_2$) and incubated for 30 min at RT before gently rinsing with PBS repeatedly. During washing steps, the disruption of the lipid bilayer was minimized by retaining approximately 200 µl of PBS in each well. Lateral mobility of the freshly prepared SLB was confirmed by adding 10 µg/ml of fluorescently labeled streptavidin (Invitrogen, S11223) and monitoring fluorescence recovery after photobleaching (FRAP) as described elsewhere (*35*). Excess Ca^{2+} ions in the system were removed by adding 0.5 mM of EDTA followed by gently rinsing with MilliQ water. The NTA groups in DGS-NTA(Ni) lipids were then recharged by adding 1 mM of $NiCl_2$ for 15 min and gently rinsed with PBS repeatedly. Finally, SLB was blocked with 5% BSA in PBS for 15 min at RT.

T cell activation on SLB

To decorate the SLB with biotinylated pMHC and His-tagged ICAM-1, 100 µg/ml of streptavidin (Life Technologies) was incubated for 20 min and rinsed with PBS. Afterwards, 500 ng/µl of biotinylated H-2D^b–NP$_{366}$ (pMHCI) (*12*) and 200 ng/µl of His-tagged ICAM-1 (Sino Biological) prepared in 5% BSA in PBS was added to the lipid bilayer and incubated for 1 hour at RT. SLB was gently rinsed with PBS for several times to remove excess unbound proteins. Before adding T cell hybridomas, SLB was incubated with warm DMEM culture media (37°C) for 30 min. T cell hybridomas were then allowed to activate on the lipid bilayer for 5 min at 37°C, followed by immediate cell fixation with 4% paraformaldehyde (vol/vol) in PBS for 15 min at RT. Excess fixatives were removed by rinsing with PBS afterwards.

Immunostaining of 5KC T cells

Prior to immunostaining 5KC T cells were permeabilized with 0.1% Triton X-100 (vol/vol) (Sigma-Aldrich) for 15 min and then rinsed with PBS. Cells were then blocked with 5% BSA in PBS for 1 hour. T cells were stained with primary antibodies reactive against TCRβ subunit and conjugated to Alexa Fluor 647 fluorophore (BioLegend). Cells were probed with primary antibodies for 1 hour at RT. Following antibody staining, samples were repeatedly rinsed with PBS to remove excess unbound antibodies and fluorophores. A post-fixation was performed using 4% paraformaldehyde (vol/vol) in PBS for 15 min. Prior to imaging, 0.1-µm TetraSpeck microspheres (Invitrogen) were embedded on to the lipid bilayer.

Single-molecule localization microscopy with *d*STORM

For single-molecule imaging, an imaging buffer consisting of TN buffer (50 mM Tris-HCl [pH 8.0], 10 mM NaCl), oxygen scavenger system GLOX (0.5 mg/ml glucose oxidase, G2133, Sigma-Aldrich; 40 µg/ml catalase, C-100, Sigma-Aldrich; and 10% w/v glucose), and 10 mM 2-aminoethanethiol (MEA: M6500, Sigma-Aldrich) was used. *d*STORM image sequences were acquired on a total internal reflection fluorescence (TIRF) microscope (commercial setup, Zeiss Elyra) with a 100X oil-immersion objective (NA = 1.46). For Alexa Fluor 647, 633 nm (15 mW) laser illumination was used alongside with a 405-nm activator laser (15 µW) for imaging. Time series of 10,000 frames were acquired per sample with a cooled, electron-multiplying charge-coupled device camera (iXon DU-897D; Andor) with an exposure time of 50 ms. Image processing, including fiducial markers-based drift correction and generation of *x*–*y* particle coordinates for each molecule detected in the acquisition were performed by Zeiss Zen software (Zen Black 2012 version).

Expression, refolding, purification, crystallization, and structure determination

DNA fragments encoding the TCRα-variable (TRAV) and TCRβ-variable (TRBV) segments of the B17.C1 TCR were purchased, codon optimized (Genscript), amplified and cloned separately into a previously reported expression vector fused to human Cα and Cβ, respectively (*12*). The B17.R2 TCR was generated by mutagenesis of the B17.R1 TCR. The B13.C1 TCRαβ construct was purchased, codon optimized for mammalian cell expression (Genscript) and cloned into a pHLsec vector. Each TCR is a chimeric construct of mouse variable and human constant domain. The plasmids constructs were confirmed via DNA sequencing. The B13.C1 TCR was produced in HEK293S cells as a soluble protein, purified via its His tag over affinity column, and size exclusion chromatography. Soluble H-2D^b WT or mutant heavy chain (generated by site direct mutagenesis), the human and mouse β2m, the B17.R1, B17.R2 and the B17.C1 TCRs α and β chains were expressed separately in *E. coli* (Novagen 70236) as inclusion bodies then subsequently solubilized, refolded, and purified as previously reported (*12*).

Crystals of the ternary B17.R2–H-2D^b–NP$_{366}$ complex were grown by the hanging-drop, vapor-diffusion method at 20°C with a protein/reservoir drop ratio of 1:1, at 3 mg/ml in 10 mM Tris-HCl pH 8.0, 150 mM NaCl using 20% PEG 3350, 0.2 M K/Na/Tartrate, and 0.1 M Bis-tris-Propane buffer pH 6.5. Crystals of the ternary B17.C1–H-2D^b–NP$_{366}$ complex were grown by the hanging-drop, vapor-diffusion method at 20°C with a protein/reservoir drop ratio of 1:1, at 8 mg/ml in 10 mM Tris-HCl pH 8.0, 150 mM NaCl using 16% PEG 3350, 0.2 M potassium thiocyanide, 4% ethylene glycol, and 0.1 M Bis-tris-propane buffer pH 7.6. The crystals were soaked in a cryoprotectant solution containing mother liquor solution with the PEG concentration increased to 30% (w/v) and then flash-frozen in liquid nitrogen.

For the B17.C1–H-2D^b–NP$_{366}$ structure, despite successfully reproducing and testing numerous crystals, only a single crystal gave a diffraction at high resolution (i.e. <5 Å) and was rapidly destroyed by radiation damage. Datasets were collected on the MX1 (*51*) and MX2

(*52*) beamline at the Australian Synchrotron (Clayton, Victoria, Australia), processed using XDS software (*53*) and scaled using Aimless software (*54*) from the CCP4 suite (*55*). The data cut-off used was $CC_{1/2}>0.5\%$ and $I/\sigma(I)>1.5$ (*56*). The structures were determined by molecular replacement using the PHASER program (*57*) with the B17.R1 TCR from the previous B17.R1–H-2D^b–NP$_{366}$ complex as the search model for the TCR (PDB accession code 5SWZ (*12*)). Manual model building was conducted using the Coot software (*58*) followed by maximum-likelihood refinement with the Buster program (*59*). The final model has been validated using the PDB validation web site and the final refinement statistics are summarized in table S1. The electron density at the interface was well defined despite a slightly above average R factors. The high R factors are due to poor electron density for some parts of H2D^b α3 domain, the β2m, as well as the C-terminus of TCRα constant domain. These regions are distal from the ligand interface however. All molecular graphics representations were created using PyMol (The PyMOL Molecular Graphics System, Version 2.0 Schrödinger, LLC). The structures have been deposited into the PDB database (B17.R2 TCR–H-2D^b–NP$_{366}$, PDB 7JWI; B17.C1 TCR–H-2D^b–NP$_{366}$, PDB 7JWJ).

Surface plasmon resonance

Surface plasmon resonance experiments were conducted at 25°C on the BIAcore T200 and BIAcore 3000 instrument (GE Healthcare, Buckinghamshire, UK) with 10 mM Tris-HCl (pH 8), 150 mM NaCl, 0.005% surfactant P20, and 0.5% BSA buffer. The 12H8 antibody was bound to all flow cells of a CM5 sensor chip via amine coupling (*60*), and all TCRs subsequently bind to the antibody. A negative control (LC13 TCR) (*61*) was used on each SPR chip bound to flow cell 1. Each cycle of TCR injection and pMHC injection was regenerated with Actisep (Sterogene). pMHC was flowed over the surface with a concentration range of 0.78–200 μM at a flow rate of 5 μl/min or 30 μl/min. A minimum of two independent experiments were conducted (n=2) in duplicate. GraphPad Prism software was used for data analysis with the 1:1 Langmuir binding model.

Statistical analyses

Statistical analysis was performed with one way ANOVA or two-way ANOVA when comparing multiple groups as indicated. For data obtained over multiple days we considered the possibility of day to day variation which we accounted for as a “nuisance factor” in the two-way ANOVA. We did not find a statistically significant effect of day to day variation in our analysis. Where appropriate we also performed paired samples t-tests as indicated in the figure legends which pairs the data-set by the day in which they were obtained; p values are denoted as * $P \leq 0.05$, ** $P \leq 0.01$, *** $P \leq 0.001$, and **** $P \leq 0.0001$. Ripley’s K analysis was used to quantify the degree of clustering in a population of molecules compared to a complete spatial randomness (*62*). For each molecule registered as a localization event, Ripley’s (K) calculates the number of neighbouring localizations within a given radius (r) corrected by the total density of localizations providing information on the degree of spatial clustering of molecules within a region of interest (ROI). In this study, we performed Ripley’s K analysis on single-molecule images using a previously published algorithm (*27*). To determine the average clustering value within a ROI, this algorithm utilized a linearized form of Ripley’s (K), the $L(r)-r$. Here, r is defined as the spatial scale radius. In a complete spatial randomness, $L(r)-r$ value equaled zero. Similarly, a positive value for $L(r)-r$ at a given r radius indicated a clustering of localization events, whereas a negative value represented a dispersed spatial organization (negative clustering). The start (0 nm), end (500 nm), and step size (10 nm) for r in the algorithm were user defined. The maximum $L(r)-r$ value derived from $L(r)-r$ vs r graph corresponded to the spatial scale (r) at which the highest degree of clustering of localizations was observed.

References and Notes

1. J. Rossjohn, S. Gras, J. J. Miles, S. J. Turner, D. I. Godfrey, J. McCluskey, T cell antigen receptor recognition of antigen-presenting molecules. *Annu. Rev. Immunol.* **33**, 169–200 (2015).
2. S. Dai, E. S. Huseby, K. Rubtsova, J. Scott-Browne, F. Crawford, W. A. Macdonald, P. Marrack, J. W. Kappler, Crossreactive T Cells Spotlight the Germline Rules for αβ T Cell-Receptor Interactions with MHC Molecules. *Immunity*. **28**, 324–334 (2008).
3. D. Feng, C. J. Bond, L. K. Ely, J. Maynard, K. C. Garcia, Structural evidence for a germline-encoded T cell receptor–major histocompatibility complex interaction "codon." *Nat. Immunol.* **8**, 975–983 (2007).
4. B. D. Stadinski, P. Trenh, R. L. Smith, B. Bautista, P. G. Huseby, G. Li, L. J. Stern, E. S. Huseby, A role for differential variable gene pairing in creating T cell receptors specific for unique major histocompatibility ligands. *Immunity*. **35**, 694–704 (2011).
5. F. Van Laethem, A. N. Tikhonova, A. Singer, MHC restriction is imposed on a diverse T cell receptor repertoire by CD4 and CD8 co-receptors during thymic selection. *Trends Immunol.* **33** (2012), pp. 437–441.
6. S. Rangarajan, R. A. Mariuzza, T cell receptor bias for MHC: Co-evolution or co-receptors? *Cell. Mol. Life Sci.* **71** (2014), pp. 3059–3068.
7. N. L. La Gruta, S. Gras, S. R. Daley, P. G. Thomas, J. Rossjohn, Understanding the drivers of MHC restriction of T cell receptors. *Nat. Rev. Immunol.* **18** (2018), pp. 467–478.
8. P. Zareie, C. Farenc, N. L. La Gruta, MHC Restriction: Where Are We Now? *Viral Immunol.* **33**, 179–187 (2020).
9. D. X. Beringer, F. S. Kleijwegt, F. Wiede, A. R. Van Der Slik, K. L. Loh, J. Petersen, N. L. Dudek, G. Duinkerken, S. Laban, A. Joosten, J. P. Vivian, Z. Chen, A. P.

Uldrich, D. I. Godfrey, J. McCluskey, D. A. Price, K. J. Radford, A. W. Purcell, T. Nikolic, H. H. Reid, T. Tiganis, B. O. Roep, J. Rossjohn, T cell receptor reversed polarity recognition of a self-antigen major histocompatibility complex. *Nat. Immunol.* **16**, 1153–1161 (2015).

10. J. J. Adams, S. Narayanan, B. Liu, M. E. Birnbaum, A. C. Kruse, N. A. Bowerman, W. Chen, A. M. Levin, J. M. Connolly, C. Zhu, D. M. Kranz, K. C. Garcia, T cell receptor signaling is limited by docking geometry to peptide-major histocompatibility complex. *Immunity*. **35**, 681–693 (2011).
11. B. C. Sim, L. Zerva, M. I. Greene, N. R. J. Gascoigne, Control of MHC restriction by TCR V(α) CDR1 and CDR2. *Science (80-.).* **273**, 963–966 (1996).
12. S. Gras, J. Chadderton, C. M. Del Campo, C. Farenc, F. Wiede, T. M. Josephs, X. Y. Sng, M. Mirams, K. A. Watson, T. Tiganis, K. M. Quinn, J. Rossjohn, N. L. La Gruta, Reversed T Cell Receptor Docking on a Major Histocompatibility Class I Complex Limits Involvement in the Immune Response. *Immunity*. **45**, 749–760 (2016).
13. T. Cukalac, W. T. Kan, P. Dash, J. Guan, K. M. Quinn, S. Gras, P. G. Thomas, N. L. La Gruta, Paired TCRαβ analysis of virus-specific CD8+ T cells exposes diversity in a previously defined “Narrow” repertoire. *Immunol. Cell Biol.* **93**, 804–814 (2015).
14. J. Huang, V. I. Zarnitsyna, B. Liu, L. J. Edwards, N. Jiang, B. D. Evavold, C. Zhu, The kinetics of two-dimensional TCR and pMHC interactions determine T-cell responsiveness. *Nature*. **464**, 932–936 (2010).
15. J. J. Sabatino Jr, J. Huang, C. Zhu, B. D. Evavold, High prevalence of low affinity peptide-MHC II tetramer-negative effectors during polyclonal CD4+ T cell responses. *J. Exp. Med.* **208**, 81–90 (2011).
16. R. J. Martinez, R. Andargachew, H. A. Martinez, B. D. Evavold, Low-affinity CD4+ T cells are major responders in the primary immune response. *Nat. Commun.* **7**, 13848

(2016).

17. E. M. Kolawole, R. Andargachew, B. Liu, J. R. Jacobs, B. D. Evavold, 2D Kinetic Analysis of TCR and CD8 Coreceptor for LCMV GP33 Epitopes. *Front. Immunol.* **9**, 2348 (2018).

18. R. Andargachew, R. J. Martinez, E. M. Kolawole, B. D. Evavold, CD4 T Cell Affinity Diversity Is Equally Maintained during Acute and Chronic Infection. *J. Immunol.* **201**, 19–30 (2018).

19. T. A. Potter, T. V. Rajan, R. F. Dick, J. A. Bluestone, Substitution at residue 227 of H-2 class I molecules abrogates recognition by CD8-dependent, but not CD8-independent, cytotoxic T lymphocytes. *Nature*. **337**, 73–75 (1989).

20. L. Limozin, M. Bridge, P. Bongrand, O. Dushek, P. A. van der Merwe, P. Robert, TCR–pMHC kinetics under force in a cell-free system show no intrinsic catch bond, but a minimal encounter duration before binding. *Proc. Natl. Acad. Sci. U. S. A.* **116**, 16943–16948 (2019).

21. B. Liu, W. Chen, B. D. Evavold, C. Zhu, Accumulation of dynamic catch bonds between TCR and agonist peptide-MHC triggers T cell signaling. *Cell*. **157**, 357–368 (2014).

22. J. Hong, S. P. Persaud, S. Horvath, P. M. Allen, B. D. Evavold, C. Zhu, Force-Regulated In Situ TCR–Peptide-Bound MHC Class II Kinetics Determine Functions of CD4 + T Cells . *J. Immunol.* **195**, 3557–3564 (2015).

23. J. Holst, A. L. Szymczak-Workman, K. M. Vignali, A. R. Burton, C. J. Workman, D. A. A. Vignali, Generation of T-cell receptor retrogenic mice. *Nat. Protoc.* **1**, 406–417 (2006).

24. J. White, A. Pullen, K. Choi, P. Marrack, J. W. Kappler, Antigen recognition properties of mutant V beta 3+ T cell receptors are consistent with an

immunoglobulin-like structure for the receptor. *J. Exp. Med.* **177**, 119–125 (1993).

25. Y. Yin, X. X. Wang, R. A. Mariuzza, Crystal structure of a complete ternary complex of T-cell receptor, peptide-MHC, and CD4. *Proc. Natl. Acad. Sci. U. S. A.* **109**, 5405–5410 (2012).

26. R. Wang, K. Natarajan, D. H. Margulies, Structural Basis of the CD8αβ/MHC Class I Interaction: Focused Recognition Orients CD8β to a T Cell Proximal Position. *J. Immunol.* **183**, 2554–2564 (2009).

27. S. V. Pageon, P. R. Nicovich, M. Mollazade, T. Tabarin, K. Gaus, Clus-DoC: A combined cluster detection and colocalization analysis for single-molecule localization microscopy data. *Mol. Biol. Cell*. **27**, 3627–3636 (2016).

28. D. Dong, L. Zheng, J. Lin, B. Zhang, Y. Zhu, N. Li, S. Xie, Y. Wang, N. Gao, Z. Huang, Structural basis of assembly of the human T cell receptor–CD3 complex. *Nature*. **573**, 546–552 (2019).

29. T. Zal, M. A. Zal, N. R. J. Gascoigne, Inhibition of T cell receptor-coreceptor interactions by antagonist ligands visualized by live FRET imaging of the T-hybridoma immunological synapse. *Immunity*. **16**, 521–534 (2002).

30. A. N. Tikhonova, F. Van Laethem, K. I. Hanada, J. Lu, L. A. Pobezinsky, C. Hong, T. I. Guinter, S. K. Jeurling, G. Bernhardt, J. H. Park, J. C. Yang, P. D. Sun, A. Singer, αβ T Cell Receptors that Do Not Undergo Major Histocompatibility Complex-Specific Thymic Selection Possess Antibody-like Recognition Specificities. *Immunity*. **36**, 79–91 (2012).

31. P. P. Yachi, J. Ampudia, N. R. J. Gascoigne, T. Zal, Nonstimulatory peptides contribute to antigen-induced CD8-T cell receptor interaction at the immunological synapse. *Nat. Immunol.* **6**, 785–792 (2005).

32. J. Casas, J. Brzostek, V. I. Zarnitsyna, J. S. Hong, Q. Wei, J. A. H. Hoerter, G. Fu, J.

Ampudia, R. Zamoyska, C. Zhu, N. R. J. Gascoigne, Ligand-engaged TCR is triggered by Lck not associated with CD8 coreceptor. *Nat. Commun.* **5** (2014).

33. J. M. Turner, M. H. Brodsky, B. A. Irving, S. D. Levin, R. M. Perlmutter, D. R. Littman, Interaction of the unique N-terminal region of tyrosine kinase p56lck with cytoplasmic domains of CD4 and CD8 is mediated by cysteine motifs. *Cell*. **60**, 755–765 (1990).

34. M. E. Birnbaum, R. Berry, Y. S. Hsiao, Z. Chen, M. A. Shingu-Vazquez, X. Yu, D. Waghray, S. Fischer, J. McCluskey, J. Rossjohn, T. Walz, K. C. Garcia, Molecular architecture of the αβ T cell receptor-CD3 complex. *Proc. Natl. Acad. Sci. U. S. A.* **111**, 17576–17581 (2014).

35. S. V Pageon, T. Tabarin, Y. Yamamoto, Y. Ma, J. S. Bridgeman, A. Cohnen, C. Benzing, Y. Gao, M. D. Crowther, K. Tungatt, G. Dolton, A. K. Sewell, D. A. Price, O. Acuto, R. G. Parton, J. J. Gooding, J. Rossy, J. Rossjohn, K. Gaus, Functional role of T-cell receptor nanoclusters in signal initiation and antigen discrimination. *Proc. Natl. Acad. Sci. U. S. A.* **113**, E5454–E5463 (2016).

36. F. Van Laethem, S. D. Sarafova, J. H. Park, X. Tai, L. Pobezinsky, T. I. I. Guinter, S. Adoro, A. Adams, S. O. Sharrow, L. Feigenbaum, A. Singer, Deletion of CD4 and CD8 Coreceptors Permits Generation of αβT Cells that Recognize Antigens Independently of the MHC. *Immunity*. **27**, 735–750 (2007).

37. F. Van Laethem, A. N. Tikhonova, L. A. Pobezinsky, X. Tai, M. Y. Kimura, C. Le Saout, T. I. Guinter, A. Adams, S. O. Sharrow, G. Bernhardt, L. Feigenbaum, A. Singer, Lck availability during thymic selection determines the recognition specificity of the T cell repertoire. *Cell*. **154**, 1326 (2013).

38. M. Hahn, M. J. Nicholson, J. Pyrdol, K. W. Wucherpfennig, Unconventional topology of self peptide-major histocompatibility complex binding by a human autoimmune T

cell receptor. *Nat. Immunol.* **6**, 490–496 (2005).

39. D. K. Sethi, D. A. Schubert, A. K. Anders, A. Heroux, D. A. Bonsor, C. P. Thomas, E. J. Sundberg, J. Pyrdol, K. W. Wucherpfennig, A highly tilted binding mode by a self-reactive T cell receptor results in altered engagement of peptide and MHC. *J. Exp. Med.* **208**, 91–102 (2011).

40. Q. Wei, J. Brzostek, S. Sankaran, J. Casas, L. S. Q. Hew, J. Yap, X. Zhao, L. Wojciech, N. R. J. Gascoigne, Lck bound to coreceptor is less active than free Lck. *Proc. Natl. Acad. Sci. U. S. A.* **117**, 15809–15817 (2020).

41. V. Horkova, A. Drobek, D. Mueller, C. Gubser, V. Niederlova, L. Wyss, C. G. King, D. Zehn, O. Stepanek, Dynamics of the Coreceptor-LCK Interactions during T Cell Development Shape the Self-Reactivity of Peripheral CD4 and CD8 T Cells. *Cell Rep.* **30**, 1504-1514.e7 (2020).

42. D. L. Wiest, L. Yuan, J. Jefferson, P. Benveniste, M. Tsokos, R. D. Klausner, L. H. Glimcher, L. E. Samelson, A. Singer, Regulation of T cell receptor expression in immature CD4+CD8+ thymocytes by p56lck tyrosine kinase: basis for differential signaling by CD4 and CD8 in immature thymocytes expressing both coreceptor molecules. *J. Exp. Med.* **178**, 1701–1712 (1993).

43. H. Sanabria, D. Rodnin, K. Hemmen, T. O. Peulen, S. Felekyan, M. R. Fleissner, M. Dimura, F. Koberling, R. Kühnemuth, W. Hubbell, H. Gohlke, C. A. M. Seidel, Resolving dynamics and function of transient states in single enzyme molecules. *Nat. Commun.* **11**, 1725–1728 (2020).

44. J. Lu, F. Van Laethem, A. Bhattacharya, M. Craveiro, I. Saba, J. Chu, N. C. Love, A. Tikhonova, S. Radaev, X. Sun, A. Ko, T. Arnon, E. Shifrut, N. Friedman, N. P. Weng, A. Singer, P. D. Sun, Molecular constraints on CDR3 for thymic selection of MHC-restricted TCRs from a random pre-selection repertoire. *Nat. Commun.* (2019),

doi:10.1038/s41467-019-08906-7.

45. G. M. Davey, S. L. Schober, B. T. Endrizzi, A. K. Dutcher, S. C. Jameson, K. A. Hogquist, Preselection thymocytes are more sensitive to T cell receptor stimulation than mature T cells. *J. Exp. Med.* **188**, 1867–1874 (1998).

46. K. A. Hogquist, S. C. Jameson, W. R. Heath, J. L. Howard, M. J. Bevan, F. R. Carbone, T cell receptor antagonist peptides induce positive selection. *Cell*. **76**, 17–27 (1994).

47. K. A. Hogquist, S. C. Jameson, The self-obsession of T cells: how TCR signaling thresholds affect fate "decisions" and effector function. *Nat. Immunol.* **15**, 815–823 (2014).

48. B. Lucas, I. Štefanová, K. Yasutomo, N. Dautigny, R. N. Germain, Divergent changes in the sensitivity of maturing T cells to structurally related ligands underlies formation of a useful T cell repertoire. *Immunity*. **10**, 367–376 (1999).

49. N. L. La Gruta, W. T. Rothwell, T. Cukalac, N. G. Swan, S. A. Valkenburg, K. Kedzierska, P. G. Thomas, P. C. Doherty, S. J. Turner, Primary CTL response magnitude in mice is determined by the extent of naive T cell recruitment and subsequent clonal expansion. *J. Clin. Invest.* (2010), doi:10.1172/JCI41538.

50. J. J. Moon, H. H. Chu, M. Pepper, S. J. McSorley, S. C. Jameson, R. M. M. Kedl, M. K. Jenkins, Naive CD4+ T Cell Frequency Varies for Different Epitopes and Predicts Repertoire Diversity and Response Magnitude. *Immunity* (2007), doi:10.1016/j.immuni.2007.07.007.

51. N. P. Cowieson, D. Aragao, M. Clift, D. J. Ericsson, C. Gee, S. J. Harrop, N. Mudie, S. Panjikar, J. R. Price, A. Riboldi-Tunnicliffe, R. Williamson, T. Caradoc-Davies, MX1: a bending-magnet crystallography beamline serving both chemical and macromolecular crystallography communities at the Australian Synchrotron. *J.*

Synchrotron Radiat. **22**, 187–190 (2015).

52. D. Aragão, J. Aishima, H. Cherukuvada, R. Clarken, M. Clift, N. P. Cowieson, D. J. Ericsson, C. L. Gee, S. Macedo, N. Mudie, S. Panjikar, J. R. Price, A. Riboldi-Tunnicliffe, R. Rostan, R. Williamson, T. T. Caradoc-Davies, MX2: a high-flux undulator microfocus beamline serving both the chemical and macromolecular crystallography communities at the Australian Synchrotron. *J. Synchrotron Radiat.* **25**, 885–891 (2018).
53. W. Kabsch, XDS. *Acta Crystallogr. D. Biol. Crystallogr.* **66**, 125–132 (2010).
54. P. R. Evans, G. N. Murshudov, How good are my data and what is the resolution? *Acta Crystallogr. Sect. D Biol. Crystallogr.* **69**, 1204–1214 (2013).
55. M. D. Winn, C. C. Ballard, K. D. Cowtan, E. J. Dodson, P. Emsley, P. R. Evans, R. M. Keegan, E. B. Krissinel, A. G. W. Leslie, A. McCoy, S. J. McNicholas, G. N. Murshudov, N. S. Pannu, E. A. Potterton, H. R. Powell, R. J. Read, A. Vagin, K. S. Wilson, Overview of the CCP4 suite and current developments. *Acta Crystallogr. D. Biol. Crystallogr.* **67**, 235–242 (2011).
56. P. A. Karplus, K. Diederichs, Linking crystallographic model and data quality. *Science*. **336**, 1030–1033 (2012).
57. A. J. McCoy, R. W. Grosse-Kunstleve, P. D. Adams, M. D. Winn, L. C. Storoni, R. J. Read, Phaser crystallographic software. *J. Appl. Crystallogr.* **40**, 658–674 (2007).
58. P. Emsley, B. Lohkamp, W. G. Scott, K. Cowtan, Features and development of Coot. *Acta Crystallogr. Sect. D Biol. Crystallogr.* **66**, 486–501 (2010).
59. G. Bricogne, E. Blanc, M. Brandl, C. Flensbueg, P. Keller, W. Paciorek, P. Roversi, A. Sharff, O. S. Smart, C. Vonrhein, T. O. Womack, BUSTER version 1.10.0. *Cambridge, United Kingdom Glob. Phasing Ltd.* (2011).
60. N. A. Borg, L. K. Ely, T. Beddoe, W. A. Macdonald, H. H. Reid, C. S. Clements, A.

W. Purcell, L. Kjer-Nielsen, J. J. Miles, S. R. Burrows, J. McCluskey, J. Rossjohn, The CDR3 regions of an immunodominant T cell receptor dictate the “energetic landscape” of peptide-MHC recognition. *Nat. Immunol.* **6**, 171–180 (2005).

61. L. Kjer-Nielsen, C. S. Clements, A. W. Purcell, A. G. Brooks, J. C. Whisstock, S. R. Burrows, J. McCluskey, J. Rossjohn, A structural basis for the selection of Dominant αβ T cell receptors in antiviral immunity. *Immunity*. **18**, 53–64 (2003).

62. B. D. Ripley, Tests of “Randomness” for Spatial Point Patterns. *J. R. Stat. Soc. Ser. B*. **41**, 368–374 (1979).

Acknowledgements

We wish to dedicate this work to the memory of our coauthor and close colleague, Professor Katharina Gaus. The authors wish to thank Dr P. Marrack (National Jewish Health, Colorado) and Dr D. Vignali (University of Pittsburgh) for provision of reagents, and D. Jayasinghe, and Dr F. Weide for technical assistance. We thank Dr Paul Harrison from the Monash Bioinformatics Platform for assistance with statistical analyses. We thank the staff at Monash FlowCore, Monash Animal Resource Platform, Monash Macromolecular Crystallization Facility, Monash Micro Imaging Platforms, and the ANSTO Australian Synchrotron MX1/MX2 beamline scientists. **Funding:** The authors wish to acknowledge funding from the Australian Research Council (ARC) (DP170103631 to N.L.L and S.G., DP201102776 to N.L.L., CE140100011 to J.R. and K.G.), the National Health and Medical Research Council of Australia (NHMRC) (APP1182086 to N.L.L., APP1155162 to K.G.) and NSW Cancer Council (APP1128488 to K.G.), the Singapore Ministry of Health's National Medical Research Council under its CBRG/0097/2015 (to N.R.J.G.) and the Singapore Ministry of Education's grant (2014–T2–1–136 to N.R.J.G.). N.L.L. is supported by an ARC Future Fellowship, S.G. by an NHMRC Senior Research Fellowship, and J.R. by an ARC Laureate Fellowship. **Author Contributions:** conceptual and experimental design: N.L.L, P.Z., J.R., S.G., K.G. B.D.E., N.R.J.G.; recombinant protein expression, structure determination, and S.P.R. analyses: C.S., C.F. J.P., S.G., J.R.; generation of in vitro cell lines, retrogenic mice, FLIM-FRET imaging, assays of T cell function: P.Z. with help from C.M.J., Q.W., L.W., X.Y.X.S., A.N., C.B. and A.F., 2D measures of binding: J.R.J., E.M.K., and B.D.E.; SMLM: S.D.G and K.G.; data analysis: all authors; manuscript writing: P.Z. N.L.L., S.G., and J.R. with contributions from other authors. **Competing Interests:** The authors declare no competing interests. **Data and Materials Availability:** Structures for the B17.R2 TCR–H-2D^b–NP$_{366}$ and B17.C1 TCR–H-2D^b–NP$_{366}$ complexes have been deposited into the PDB database (B17.R2 TCR–H-2D^b–

NP_{366}, PDB 7JWI; B17.C1 TCR–H-$2D^b$–NP_{366}, PDB 7JWJ). All other data are available in the main text or the supplementary materials.

Supplementary Materials

Figures S1-S5

Tables S1-S5

Figure Legends

Fig. 1. Reverse-docking TRBV17^{+} T cells are not recruited into the immune response

(**A** and **B**) HEK293T cells were transfected with B13.C1 (black) and B17.R1 (gold) TCRs and binding of WT or mutant H-2D^{b}–NP$_{366}$ tetramers analyzed 48 hours after transfection. Live, GFP^{+} cells were gated and analyzed for change in geometric mean fluorescence intensity (geoMFI). Shown is (**A**) geoMFI as a percent change from the WT tetramer and **(B)** representative dot plots staggered (top panel) or overlaid (bottom panel) of TCR expression and binding of various mutant tetramers. Data shown in (**A**) are from two independent experiments combined. Data shown in **(B)** are dot plots from one representative experiment. (**C**) Binding response of B17.R1 TCR against H-2D^{b}–NP$_{366}^{WT}$ in black or H-2D^{b}–NP$_{366}^{A89E}$ in green. Data presented are from a single experiment representative of two independent experiments. (**D** to **K**) Representative dot plots and graphs showing the proportion of H-2D^{b}–NP$_{366}^{WT}$ binding (**D, H**, black) or H-2D^{b}–NP$_{366}^{A89E}$ binding (**E, I**, green) T cells using either TRBV13 (Vβ8.3) or TRBV17 (Vβ9) TCRβ chains isolated from naive mice (10 mice pooled/data point; **D** to **G**) or immune mice 10 days post infection (one mouse per data point; **H** to **K**). Plots represent the percentage change in TRBV13^{+} T cells bound by the H-2D^{b}–NP$_{366}^{A89E}$ tetramer relative to H-2D^{b}–NP$_{366}^{WT}$ tetramer from (**F**) naive mice and (**J**) immune mice, and the percentage change in TRBV17^{+} T cells bound by the H-2D^{b}–NP$_{366}^{A89E}$ tetramer relative to H-2D^{b}–NP$_{366}^{WT}$ tetramer binding from (**G**) naïve mice and (**K**) immune mice. Data shown from 10 pooled naïve mice in **D** to **E** represents one sample of n=3. Summary data shown in **F** and **G** are mean and SEM of three independent datasets (each containing 10 pooled mice). Data from an individual immune mouse shown in **H** and **I** represents one sample of n=9. Summary data shown in **J** and **K** are mean and SEM from a representative 3 samples (each containing one mouse) collected on one day.

Fig. 2. Prevalence of TCRs in the immune response is unrelated to TCR–pMHCI affinity

(**A** and **B**) TRBV17 TCRβ$^+$ H-2D^b–NP$_{366}$-specific TCR clonotypes presented as bar graphs with corresponding CDR3α/CDR3β sequences from (**A**) six individual naïve (m1-m6) (*13*) or (**B**) four individual immune mice (m1-m4) 10 days post infection with IAV. (**C** to **F**) HEK293T cells were transfected with pMIGII vectors encoding αβTCR and CD3γδεζ and H-2D^b–NP$_{366}$^{WT} (black) or H-2D^b–NP$_{366}$^{A89E} (green) tetramer staining analyzed by flow cytometry 48 hours later. Shown are representative flow cytometry plots of TCRβ expression and tetramer binding from live, GFP$^+$ cells (left) and SPR sensorgrams (right) of (**C**) B13.C1, (**D**) B17.C1, (**E**) B17.R2 and (**F**) B17.C2 TCRs. Data shown in C to F are from one experiment representative of two (SPR) or three (flow cytometry) independently performed experiments.

Fig. 3. B17.R2 TCR and B17.C1 TCR in complex with H-2D^b–NP$_{366}$

The TCR–pMHC complexes of (**A**) B17.R2 TCR–H-2D^b–NP$_{366}$ and (**C**) B17.C1 TCR–H-2D^b–NP$_{366}$. (**B** and **D**) The TCR atomic footprints on the surface of each corresponding pMHC complex, spheres represent the center of mass of Vα (pink) and Vβ (blue). Pie charts represent the relative contributions of each TCR segment to the pMHCI interaction, contacts are colored according to the CDR loop involved. The TCRα chain is colored pink, the TCRβ chain blue, H-2D^b white, β2m orange, and peptide black/dark gray. CDR1, 2, 3α are colored in green, teal, and purple, respectively, and CDR1, 2, 3β in red, orange, and yellow, respectively. Framework (FW) is colored pink for the FWα and blue for the FWβ.

Fig. 4. TCR–pMHCI docking orientation is a primary determinant of in vivo T cell activation and recruitment

(**A**) Schematic diagram of experimental protocol. Retrogenic CD45.2$^+$ GFP/mCherry$^+$ CD4$^-$ CD8$^+$ T cells were sorted from B13.C1 (mCherry), B17.R1 (GFP), B17.R2 (GFP) and B17.C2 (mCherry) retrogenic mice and 4×10^3 cells were transferred individually or cotransferred into naive C57BL/6 mice that were infected i.n with 1×10^4 PFU HKx31 IAV the following day. Mice were killed for analysis 10 days after infection. (**B**) Dot plots from the BAL of mice that received cotransfers of retrogenic T cells. (**C** to **N**) Shown is the percentage retrogenic CD8$^+$ T cells of total CD8$^+$ T cells isolated from the BAL (**C, F, I, L**), spleen (**D, G, J, M**) or mediastinal lymph nodes (**E, H, K, N**) from single adoptive transfers (**C** to **E**) or cotransfers (**F** to **N**) at day 10 post infection. Each point represents data from an individual mouse (n=2–8) and the combined dataset was collected over four separate days. Each sample testing cotransferred retrogenic T cells was paired with individual transfers as experimental controls.

Fig. 5. Reversed TCR–pMHCI docking does not impede TCR clustering, but mislocalizes the CD8 coreceptor and CD3 complex

(**A**) Single-molecule images of 5KC TCR transductants expressing canonical docking B13.C1 or B17.R2 TCRs on supported lipid bilayers decorated with either ICAM–1 only (ICAM–1) or ICAM–1 + H-2D^b–NP$_{366}$ (ICAM–1 + pMHC) at 5 min (scale bar: 5 µm). Close-up view of single-molecule localization microscopy image (2 µm×2 µm) as TCR cluster maps (lower panels) from representative regions (boxed, top panel), with TCRβ molecules in clusters shown in green and molecules outside clusters shown in blue. Cluster contours are highlighted in red lines. (**B**) Ripley's K analysis of TCR clustering (L(*r*)-*r*) against radii (*r*). Complete spatial randomness is shown as a solid gray line where L(*r*)-*r* = 0. Positive L(*r*)-*r* values indicate molecular clustering relative to the random distribution, shown as the mean (solid line) ± 95% CI (dashed lines) for TCRs under each condition. Dotted lines indicate ± SEM (**C**) The maximum L(*r*)-*r* value derived from the peak of the graph in (**B**) corresponds to the spatial scale (r) at which the highest degree of clustering of localizations is being observed (n=20). Statistical analysis performed by one–way ANOVA. (**D** and **E**) Representation of the TCR–CD3 complex (PDB 6JXR), CD8 coreceptor (PDB 3DMM) and ternary complex of (**D**) B17.C1 TCR–H-2D^b–NP$_{366}$ and (**E**) B17.R1 TCR–H2D^b–NP$_{366}$ (PDB 5SWZ). The different chains are shown in black for CD3ζζ, red for the CD3γε, pink for the CDδε, and blue for the TCRαβ chains. MHC is shown in white, whereas the CD8 coreceptor is shown in orange. **(F)**

DC2.4 cells labeled with cell tracker violet (CTV) were pulsed with 10 μM NP_{366} peptide for 1 hour before coculture with $5KC^{\zeta GFP.CD8\beta mCherry}$ expressing TCRs as indicated. T cell hybrids interacting with a DC2.4 cell were imaged up to 20 min post coculture by confocal microscopy and subsequently analyzed by FLIM to measure GFP lifetime 10–20 s later (fig. S3) (scale bar = 10 μm). (**G**) Amplitude weighted lifetime of GFP (T_{avAMP}) of B13.C1, B17.R1, B17.R2, B17.C1 and B17.C2 TCR^+ T cells (±NP_{366} peptide) measured as percentage change at the synapse versus non-synapse ($Syn\Delta T_{avAMP}$)**.** Cells were observed on three different days. Statistical analysis was performed by two-way ANOVA to examine the effect of stimulation and the day on which each cell was observed on the $Syn\Delta T_{avAMP}$ for each cell line. Significant effects on the $Syn\Delta T_{avAMP}$ by peptide stimulation is indicated by *** $P \leq 0.001$ as indicated. For each cell line, no significant effect on the $Syn\Delta T_{avAMP}$ was found for the day each cell was observed.

Fig. 6. Signaling constraints that mandate TCR–pMHCI docking orientation are driven by Lck sequestration and localization by the CD8 coreceptor

(**A** to **C**) Representative histograms of TCRβ expression (top panel) and dot plots of CD8αβ expression (bottom panel) by 5KC TCR transductants expressing B13.C1 (black) and B17.R2 (red). (**D, E**) Immunoblots of CD8-associated Lck in $CD8^{WT}$ $CD8^{NULL}$ and $CD8^{CxC}$ transductants expressing (**D**) B13.C1 or (**E**) B17.R2 TCRs. (**F** to **H**) Time-resolved pERK induction (top panels) up to 60 min after coincubation with peptide pulsed DC2.4 cells, presented as a percent change from a no peptide control (measured at corresponding time point) using cells that express (**F**) $CD8^{WT}$, (**G**) $CD8^{NULL}$ and (**H**) $CD8^{CxC}$. (Middle panel) pERK signal magnitude analysed by area under the curve (AUC) analysis of 0-60-mins stimulation. Samples were tested in duplicate (n=3) and mean and SEM of all datasets shown. Statistical analyses were performed using a paired samples t-test to pair by dataset. Statistical significance is indicated by ** $P \leq 0.01$ as indicated. IL-2 secretion (bottom panels) into the supernatant by (**F**)

$CD8^{WT}$, (**G**) $CD8^{NULL}$ and (**H**) $CD8^{CxC}$ transductants was measured by ELISA after 16 hours of coincubation with peptide pulsed DC2.4 cells and presented as a percentage of the plate bound anti-CD3 antibody stimulation controls. Samples were tested in duplicate (n=3) and mean and SEM of all datasets shown. Statistical analyses were performed using a paired samples t-test to pair by dataset. Statistical significance is indicated by * $P \leq 0.05$ as indicated.

Table 1. TCRs, recruitment characteristics, docking polarity and K_D

TCR	**TCRα**	**TCRβ**	**Immune Recruitment**	**Docking Polarity**	**K_D (μM) H-2$D^{bWT}$$NP_{366}$**	**K_D (μM) H-2$D^{bA89E}$$NP_{366}$**
B13.C1 (NP1–B13[#])	TRAV16; RVSGGSNAKL	TRBV13–1; SGGGNTGQL	Immuno–dominant	Canonical*	4.13 ± 1.55	ND
B17.R1 (NP1-B17[#])	TRAV14; SETSGSWQL	TRBV17; SRDLGRDTQ	Naïve or poorly recruited	Reversed	37.5 ± 4.4	>200
B17.R2	TRAV14; SETSASWQL	TRBV17; SRDLGRDTQ	Naïve or poorly recruited	Reversed	6.34 ± 1.58	62 ± 30
B17.C1	TRAV4–4; AAVTGNTGK	TRBV17; SRGTIHSNT	Clonally expanded	Canonical	>> 200	>200
B17.C2	TRAV14D; SSRRGSAK	TRBV17; SRGGLSYEQ	Clonally expanded	Canonical*	ND	ND

[#] previously reported in (*12*)

* Structure undetermined; polarity inferred by MHCI mutational analyses

ND = not determined

The SPR values are the mean ± S.E.M. of experiments done at a minimum twice in duplicate.

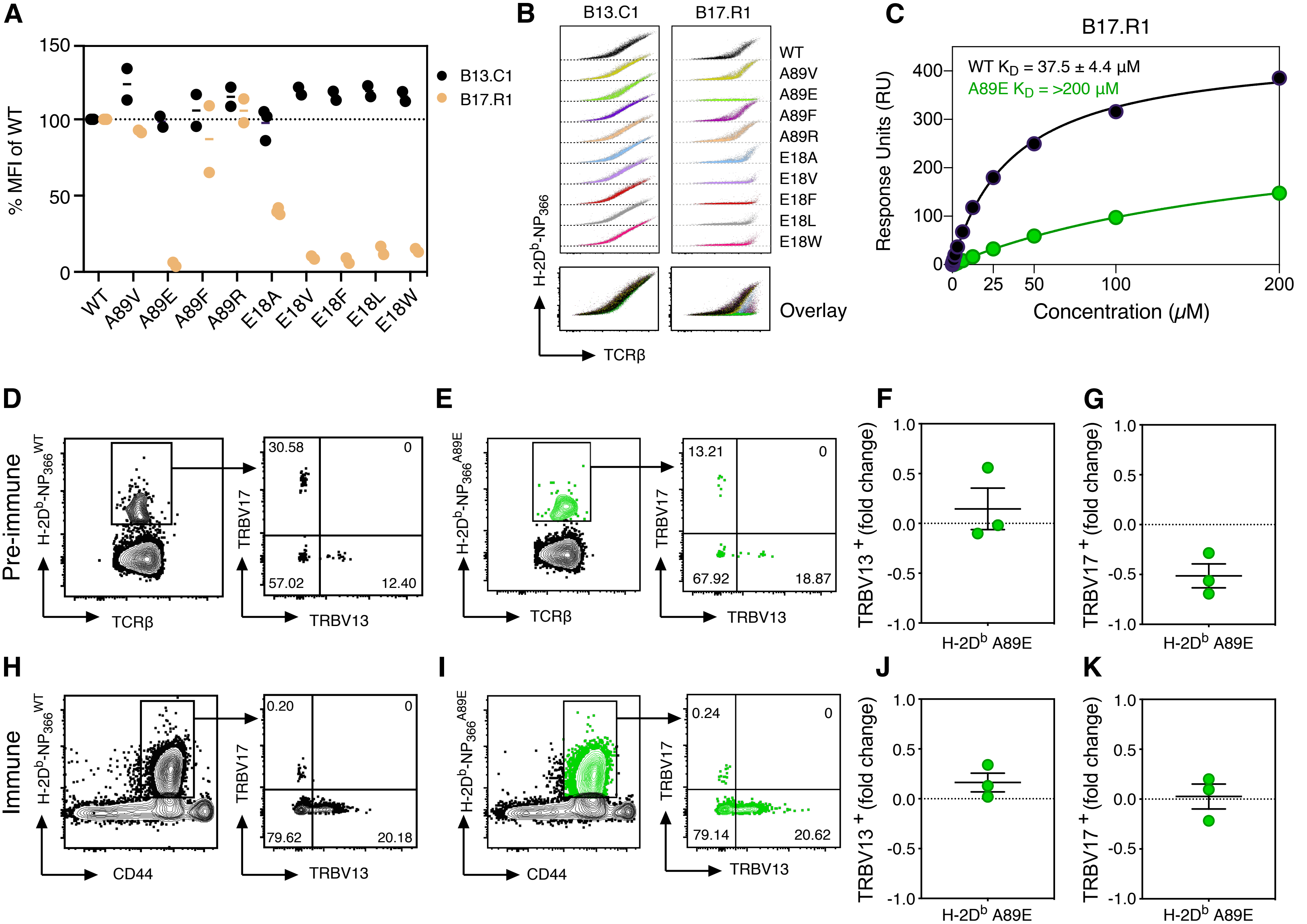
A
% MFI of WT
150
100
50
0
WT
A89V
A89E
A89F
A89R
E18A
E18V
E18F
E18L
E18W
● B13.C1
● B17.R1
B
B13.C1
B17.R1
WT
A89V
A89E
A89F
A89R
E18A
E18V
E18F
E18L
E18W
Overlay
H-2D^b-NP$_{366}$
TCRβ
C
B17.R1
WT K_D = 37.5 ± 4.4 μM
A89E K_D = >200 μM
Response Units (RU)
400
300
200
100
0
0
25
50
100
200
Concentration (μM)
D
Pre-immune
H-2D^b-NP$_{366}$^{WT}
TCRβ
TRBV17
TRBV13
30.58
0
57.02
12.40
E
H-2D^b-NP$_{366}$^{A89E}
TCRβ
TRBV17
TRBV13
13.21
0
67.92
18.87
F
TRBV13$^+$ (fold change)
1.0
0.5
0.0
-0.5
-1.0
H-2D^b A89E
G
TRBV17$^+$ (fold change)
1.0
0.5
0.0
-0.5
-1.0
H-2D^b A89E
H
Immune
H-2D^b-NP$_{366}$^{WT}
CD44
TRBV17
TRBV13
0.20
0
79.62
20.18
I
H-2D^b-NP$_{366}$^{A89E}
CD44
TRBV17
TRBV13
0.24
0
79.14
20.62
J
TRBV13$^+$ (fold change)
1.0
0.5
0.0
-0.5
-1.0
H-2D^b A89E
K
TRBV17$^+$ (fold change)
1.0
0.5
0.0
-0.5
-1.0
H-2D^b A89E

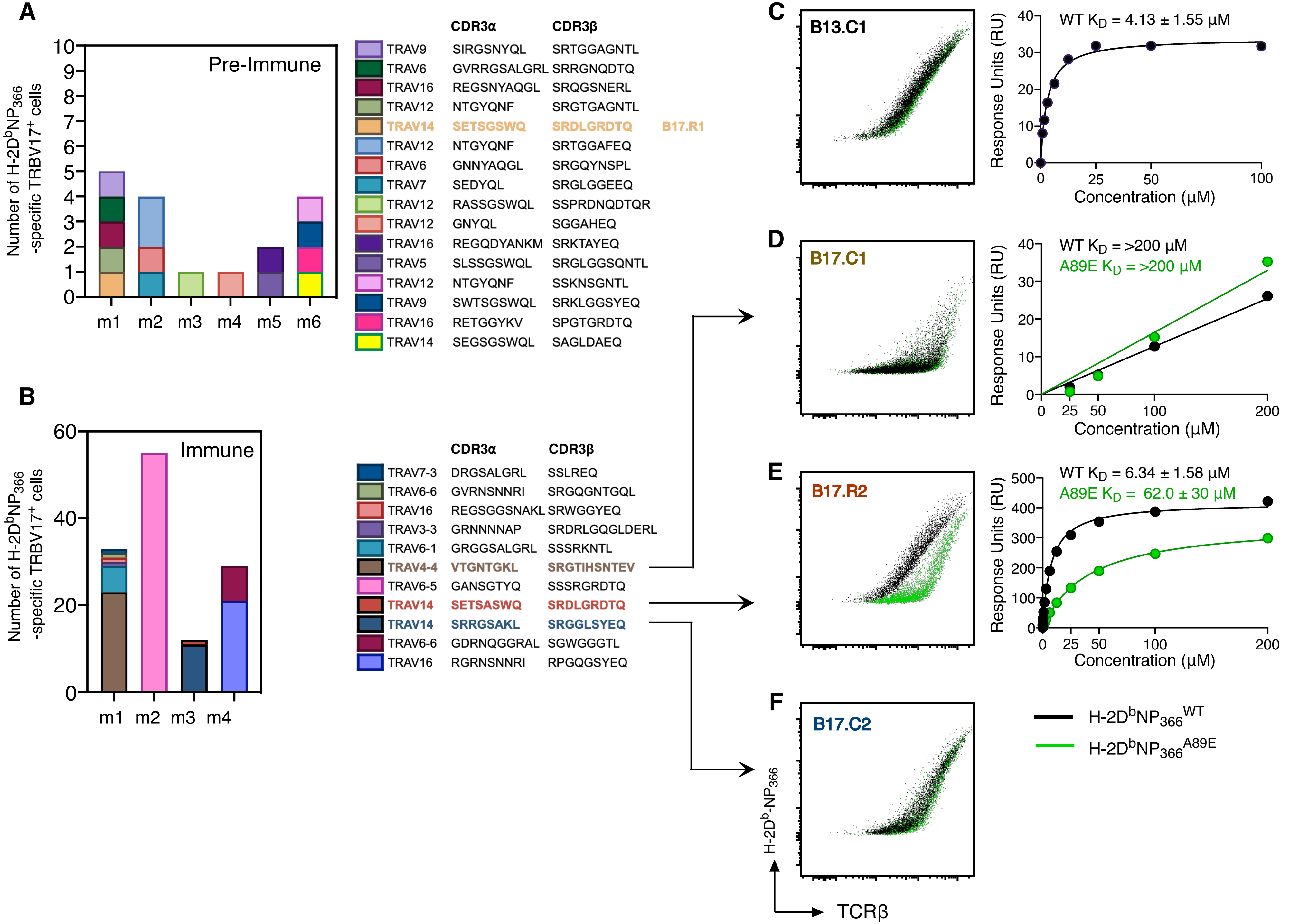

	CDR3α	CDR3β	
TRAV9	SIRGSNYQL	SRTGGAGNTL	
TRAV6	GVRRGSALGRL	SRRGNQDTQ	
TRAV16	REGSNYAQGL	SRQGSNERL	
TRAV12	NTGYQNF	SRGTGAGNTL	
TRAV14	**SETSGSWQ**	**SRDLGRDTQ**	**B17.R1**
TRAV12	NTGYQNF	SRTGGAFEQ	
TRAV6	GNNYAQGL	SRGQYNSPL	
TRAV7	SEDYQL	SRGLGGEEQ	
TRAV12	RASSGSWQL	SSPRDNQDTQR	
TRAV12	GNYQL	SGGAHEQ	
TRAV16	REGQDYANKM	SRKTAYEQ	
TRAV5	SLSSGSWQL	SRGLGGSQNTL	
TRAV12	NTGYQNF	SSKNSGNTL	
TRAV9	SWTSGSWQL	SRKLGGSYEQ	
TRAV16	RETGGYKV	SPGTGRDTQ	
TRAV14	SEGSGSWQL	SAGLDAEQ	

	CDR3α	CDR3β
TRAV7-3	DRGSALGRL	SSLREQ
TRAV6-6	GVRNSNNRI	SRGQGNTGQL
TRAV16	REGSGGSNAKL	SRWGGYEQ
TRAV3-3	GRNNNNAP	SRDRLGQGLDERL
TRAV6-1	GRGGSALGRL	SSSRKNTL
TRAV4-4	**VTGNTGKL**	**SRGTIHSNTEV**
TRAV6-5	GANSGTYQ	SSSRGRDTQ
TRAV14	**SETSASWQ**	**SRDLGRDTQ**
TRAV14	**SRRGSAKL**	**SRGGLSYEQ**
TRAV6-6	GDRNQGGRAL	SGWGGGTL
TRAV16	RGRNSNNRI	RPGQGSYEQ

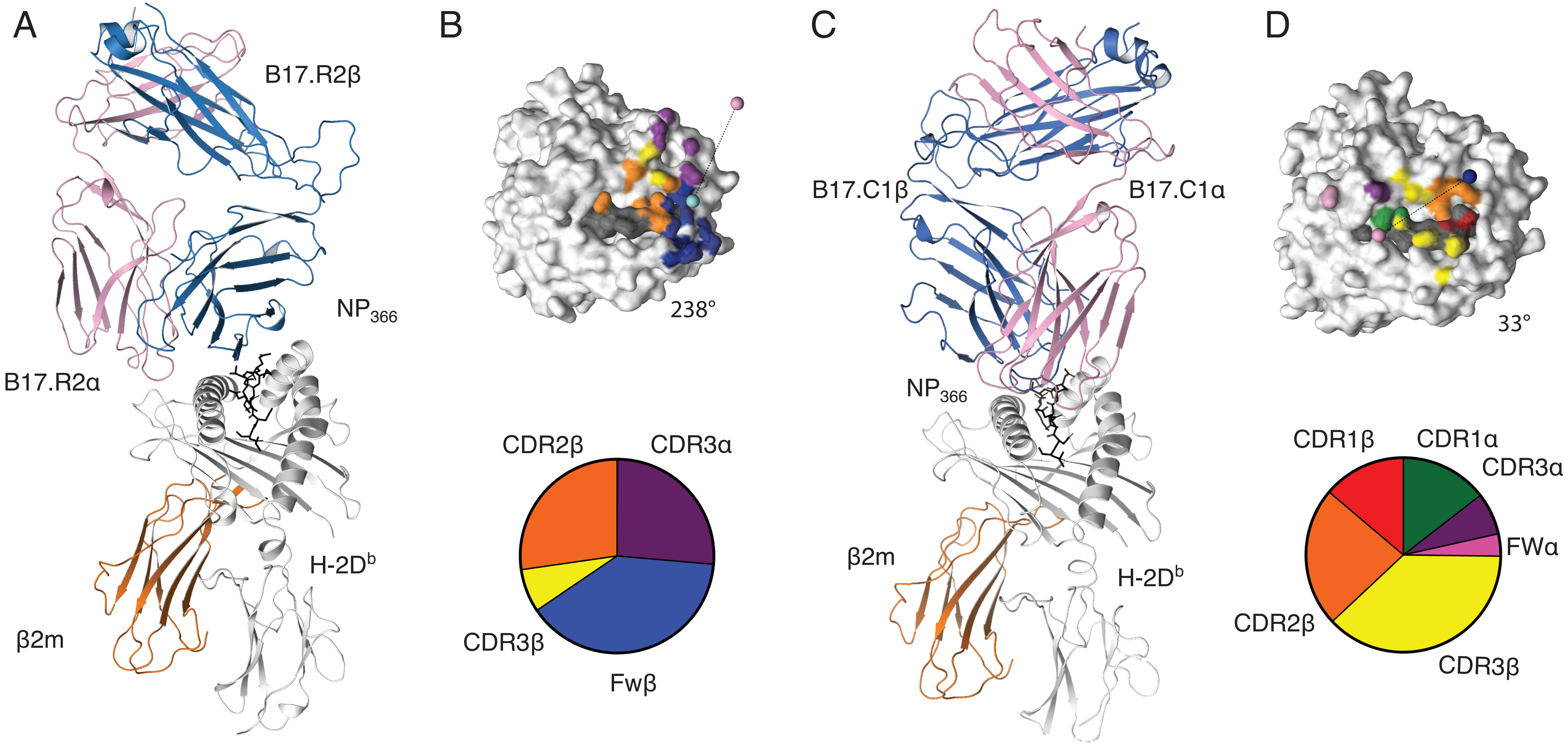
A
B17.R2β
NP$_{366}$
B17.R2α
H-2D^b
β2m
B
238°
CDR2β
CDR3α
CDR3β
Fwβ
C
B17.C1β
B17.C1α
NP$_{366}$
β2m
H-2D^b
D
33°
CDR1β
CDR1α
CDR3α
FWα
CDR2β
CDR3β

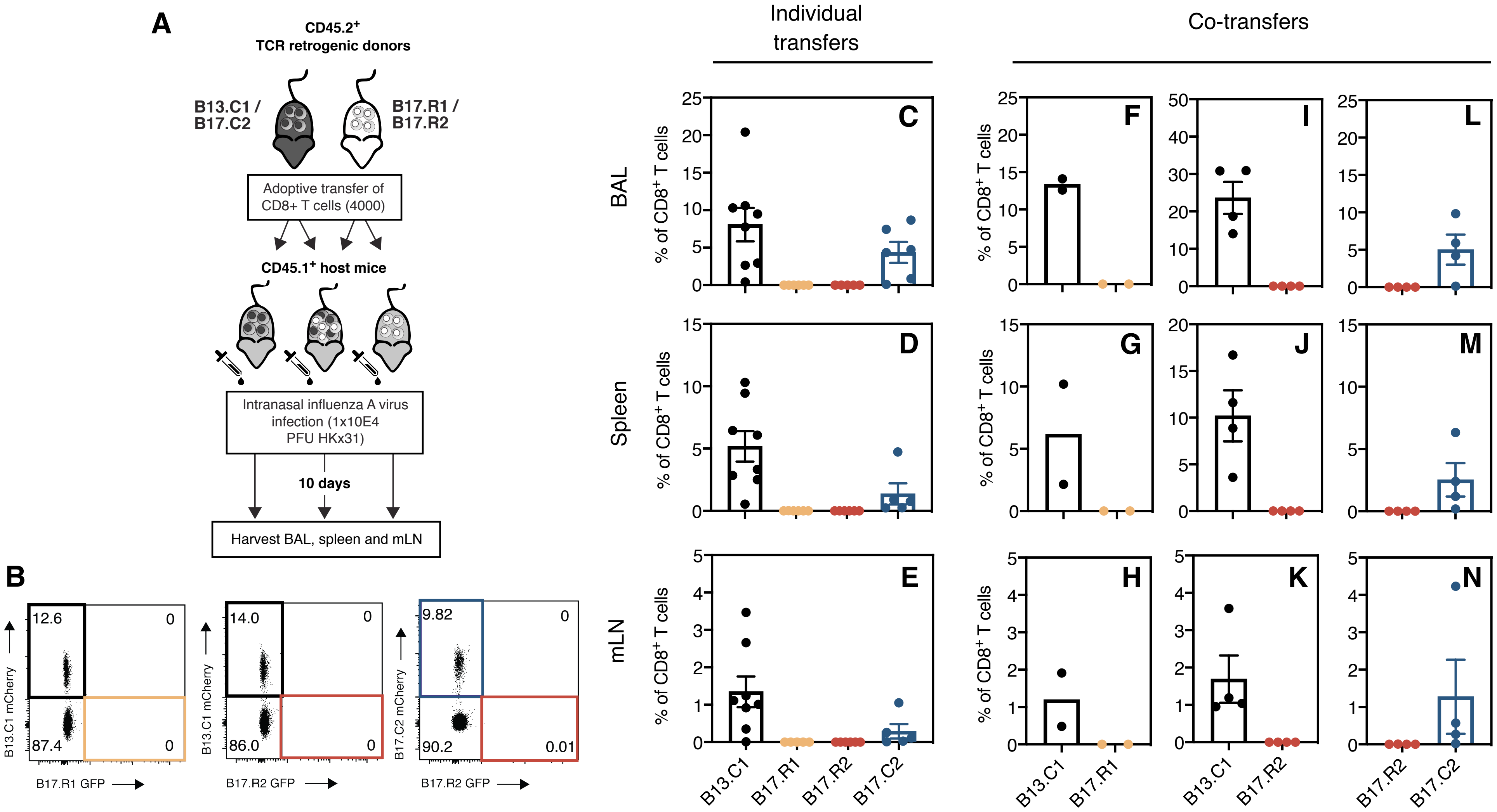
A
CD45.2+ TCR retrogenic donors
B13.C1 / B17.C2
B17.R1 / B17.R2
Adoptive transfer of CD8+ T cells (4000)
CD45.1+ host mice
Intranasal influenza A virus infection (1x10E4 PFU HKx31)
10 days
Harvest BAL, spleen and mLN
B
12.6
0
87.4
0
B13.C1 mCherry
B17.R1 GFP
14.0
0
86.0
0
B13.C1 mCherry
B17.R2 GFP
9.82
0
90.2
0.01
B17.C2 mCherry
B17.R2 GFP
Individual transfers
Co-transfers
BAL
Spleen
mLN
% of CD8+ T cells
C
D
E
F
G
H
I
J
K
L
M
N
0
5
10
15
20
25
30
40
50
1
2
3
4
B13.C1
B17.R1
B17.R2
B17.C2

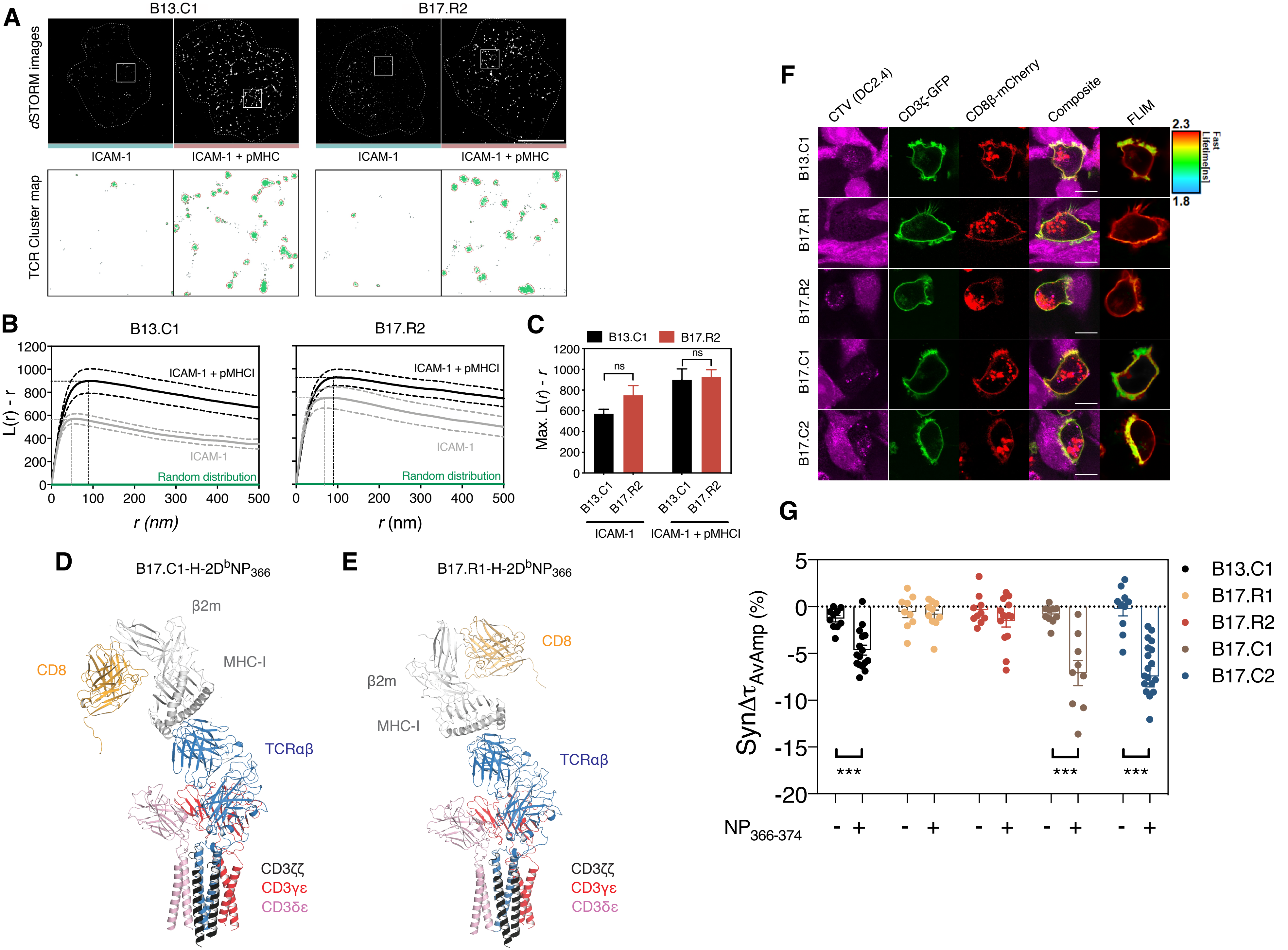
A
B13.C1
B17.R2
dSTORM images
ICAM-1
ICAM-1 + pMHC
ICAM-1
ICAM-1 + pMHC
TCR Cluster map
B
B13.C1
B17.R2
1200
1000
800
600
400
200
0
L(r) - r
ICAM-1 + pMHCI
ICAM-1
Random distribution
0 100 200 300 400 500
r (nm)
ICAM-1 + pMHCI
ICAM-1
Random distribution
0 100 200 300 400 500
r (nm)
C
B13.C1
B17.R2
Max. L(r) - r
ns
ns
B13.C1
B17.R2
B13.C1
B17.R2
ICAM-1
ICAM-1 + pMHCI
D
B17.C1-H-2DbNP366
β2m
MHC-I
CD8
TCRαβ
CD3ζζ
CD3γε
CD3δε
E
B17.R1-H-2DbNP366
CD8
β2m
MHC-I
TCRαβ
CD3ζζ
CD3γε
CD3δε
F
CTV (DC2.4)
CD3ζ-GFP
CD8β-mCherry
Composite
FLIM
B13.C1
B17.R1
B17.R2
B17.C1
B17.C2
2.3
1.8
Fast Lifetime[ns]
G
5
0
-5
-10
-15
-20
SynΔτAvAmp (%)
***
***
***
NP366-374
- + - + - + - + - +
B13.C1
B17.R1
B17.R2
B17.C1
B17.C2

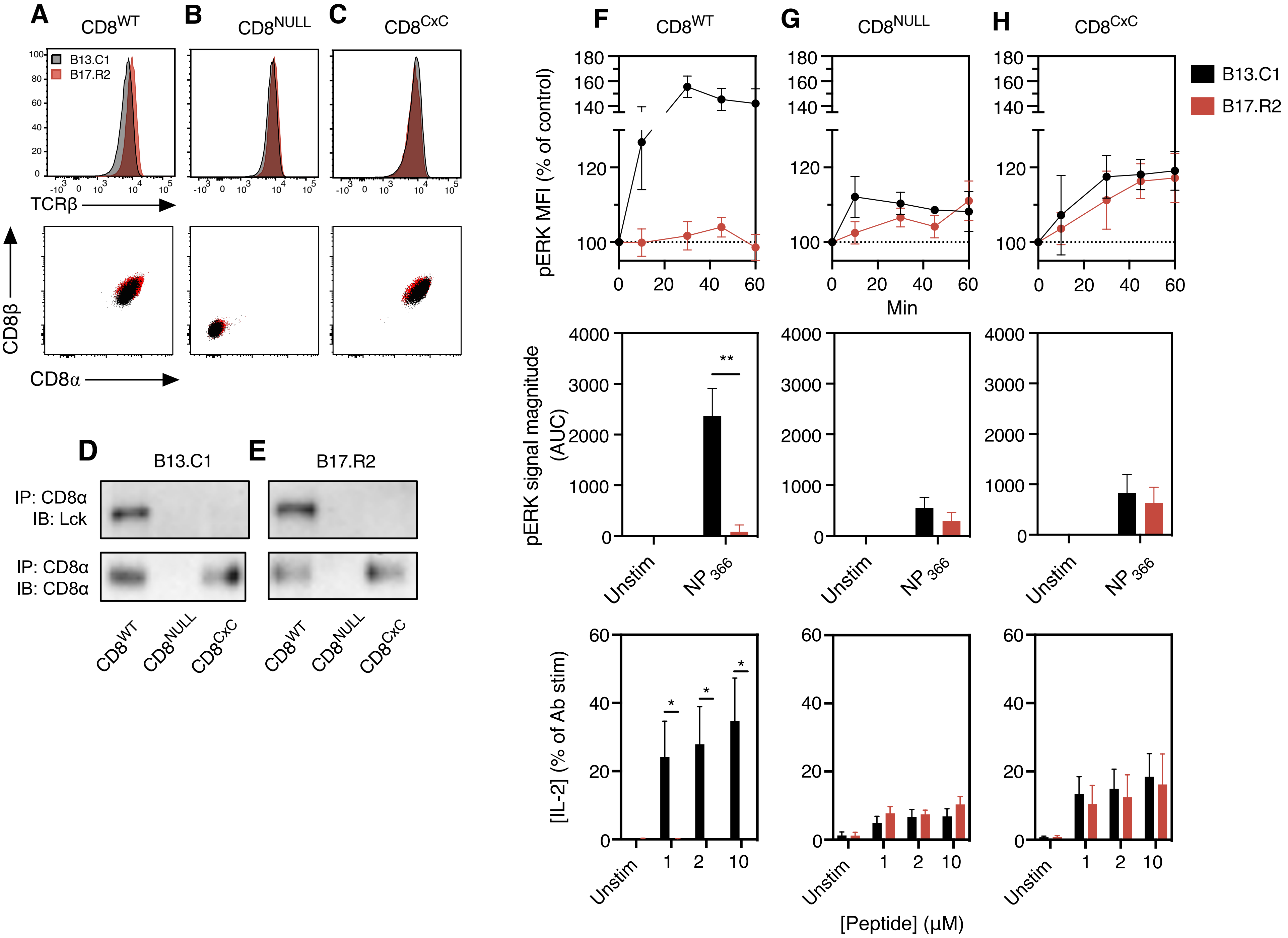
A
CD8WT
B
CD8NULL
C
CD8CxC
B13.C1
B17.R2
100
80
60
40
20
0
-10³ 0 10³ 10⁴ 10⁵
TCRβ
CD8β
CD8α
D
B13.C1
E
B17.R2
IP: CD8α
IB: Lck
IP: CD8α
IB: CD8α
CD8WT
CD8NULL
CD8CxC
F
CD8WT
G
CD8NULL
H
CD8CxC
B13.C1
B17.R2
pERK MFI (% of control)
180
160
140
120
100
0
20
40
60
Min
pERK signal magnitude (AUC)
4000
3000
2000
1000
0
**
Unstim
NP 366
[IL-2] (% of Ab stim)
60
40
20
0
*
*
*
Unstim
1
2
10
[Peptide] (µM)

Supplementary Materials for

Canonical T cell Receptor Docking on peptide–MHC is essential for T cell signaling

Pirooz Zareie[1], Christopher Szeto[1#], Carine Farenc[1], Sachith D. Gunasinghe[2], Elizabeth M. Kolawole[3], Angela Nguyen[1], Chantelle Blyth[1], Xavier Y. X. Sng[1], Jasmine Li[4], Claerwen M. Jones[1], Alex J. Fulcher[5], Jesica R. Jacobs[3], Qianru Wei[6], Lukasz Wojciech[6], Jan Petersen[1,7], Nicholas R.J. Gascoigne[6], Brian D. Evavold[3], Katharina Gaus[2], Stephanie Gras[1,7*#], Jamie Rossjohn[1,7,8*]& Nicole L. La Gruta[1*]

*Correspondence to: Nicole.la.gruta@monash.edu, Jamie.rossjohn@monash.edu, S.Gras@latrobe.edu.au

[#] Current address: Department of Biochemistry and Genetics, La Trobe Institute for Molecular Science, La Trobe University, Melbourne, Victoria, Australia

This PDF file includes:

Figs. S1 to S5

Tables S1 to S4

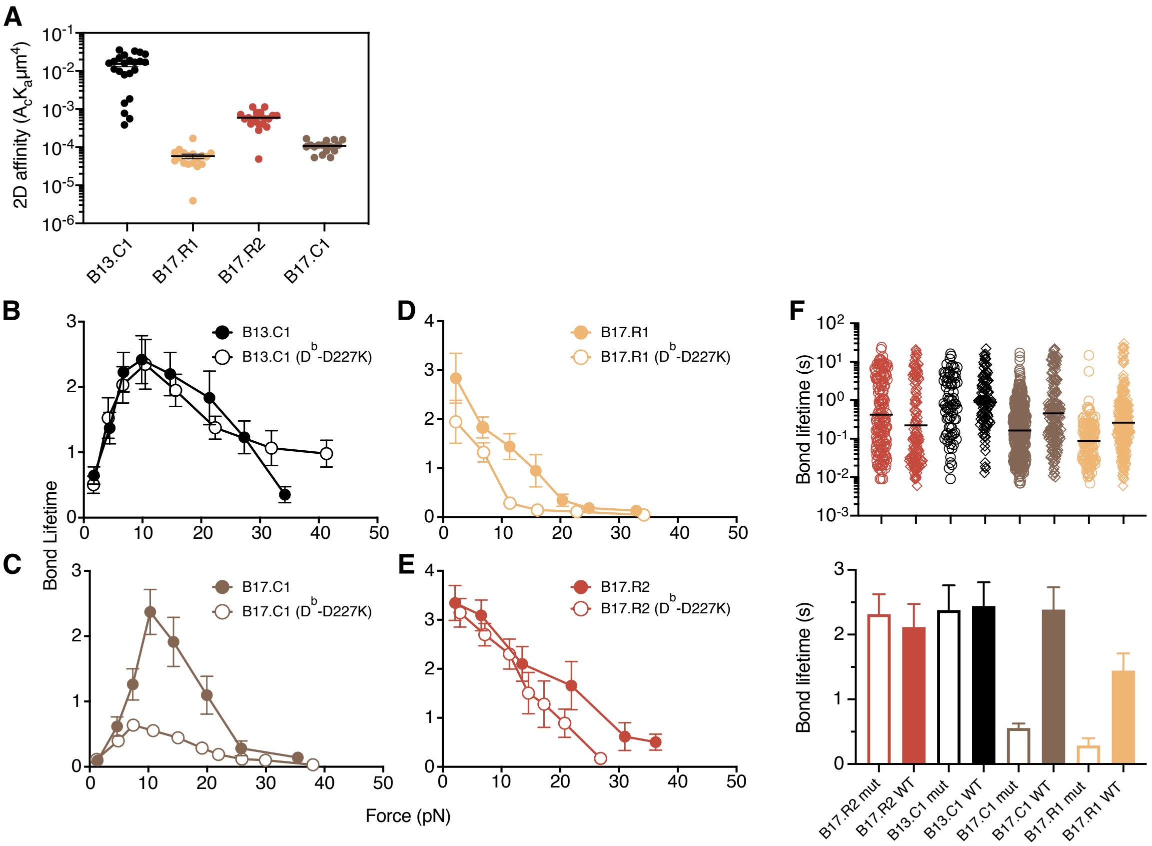

Fig. S1. Relative 2D affinity and biomembrane force probe measurements of each TCR +/- CD8 contribution to binding

(**A**) Relative 2D affinities of B13.C1, B17.R1, B17.R2 and B17.C1 to H-2DbNP$_{366}^{D227K}$ monomers were measured by 2D-MP as described. Shown are the means 2D affinity ± SEM. **B-F** Biomembrane force probe experiments were performed for B13.C1 (**B**), B17.C1 (**C**), B17.R1 (**D**) and B17.R2 (**E**) TCRs as described. (**F**) Geometric means (top panel) or mean ± SEM (bottom panel) of bond lifetimes measured at 10pN force. Shown are the means and SEM of >600 bond lifetimes from 3 experiments.

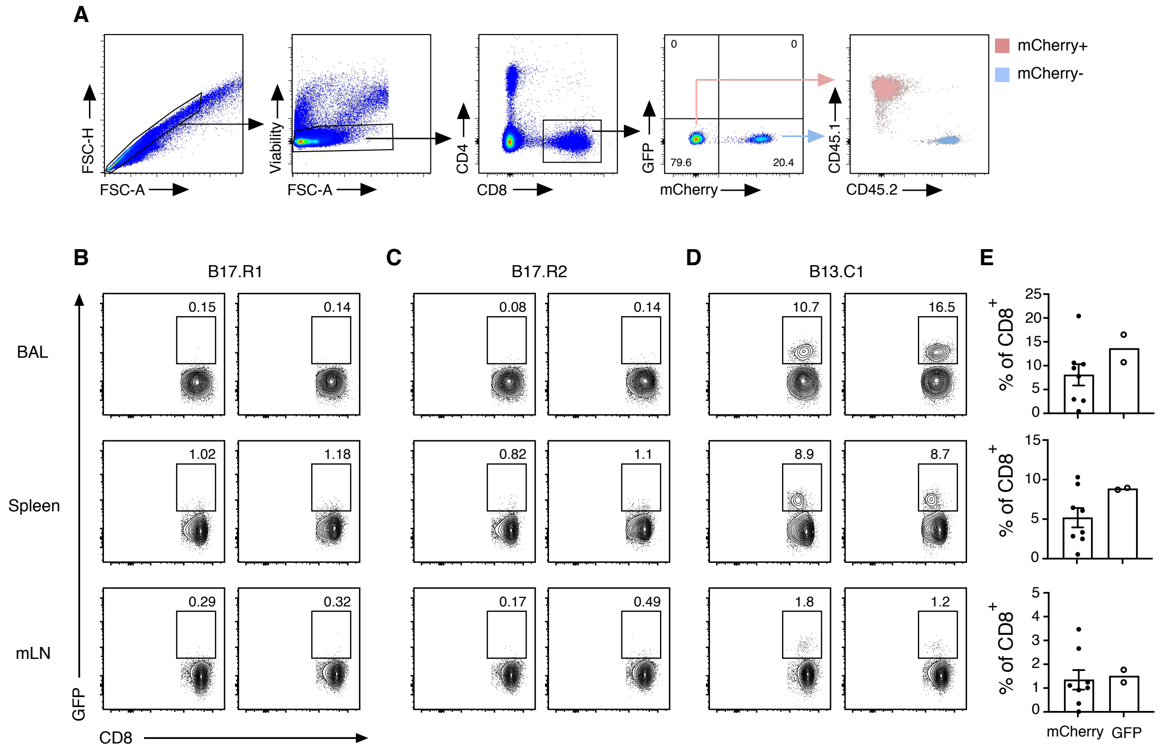

Fig. S2. Gating Strategy and Recruitment of Retrogenic CD8$^+$ T cells After Infection

CD45.1$^-$ CD45.2$^+$ CD4$^-$ CD8$^+$ GFP/mCherry$^+$ T cells were sorted from female TCR retrogenic mice using a BD FACS Aria III Fusion or BD Influx cell sorter. Retrogenic T cells (4×10^3) from each line were injected i.v. into naïve female B6.SJ$^{\text{ptprca}}$ (CD45.1) mice. The next day, mice were infected with 1×10^4 PFU HKx31 IAV and 10 days later cells mice were killed. (**A**) Cells isolated from bronchoalveolar lavage (BAL) were isolated and analyzed by flow cytometry. Shown is a representative FACS plot and gating strategy of cells isolated from the BAL of mice that received a co-transfer of B13.C1 TCR$^+$ (mCherry$^+$) and B17.R2 TCR$^+$ (GFP$^+$) T cells. (**B** to **E**) GFP expression from individual transfer of (**B**) B17.R1 TCR$^+$ (GFP$^+$), (**C**) B17.R2 TCR$^+$ (GFP$^+$) or (**D**) B13.C1 TCR$^+$ (GFP$^+$) CD8$^+$ T cells from BAL (top panel), spleen (middle panel) and mediastinal lymph nodes (mLN; bottom panel) at 10d following IAV infection; 2 mice per group. (**E**)

Comparison of recruitment of mCherry$^+$ (data from **Fig. 4**) or GFP$^+$ B13.C1 retrogenic T cells at 10d following IAV infection, as percent of CD8$^+$ T cells in the BAL (top panel), spleen (middle panel) and mLN (bottom panel).

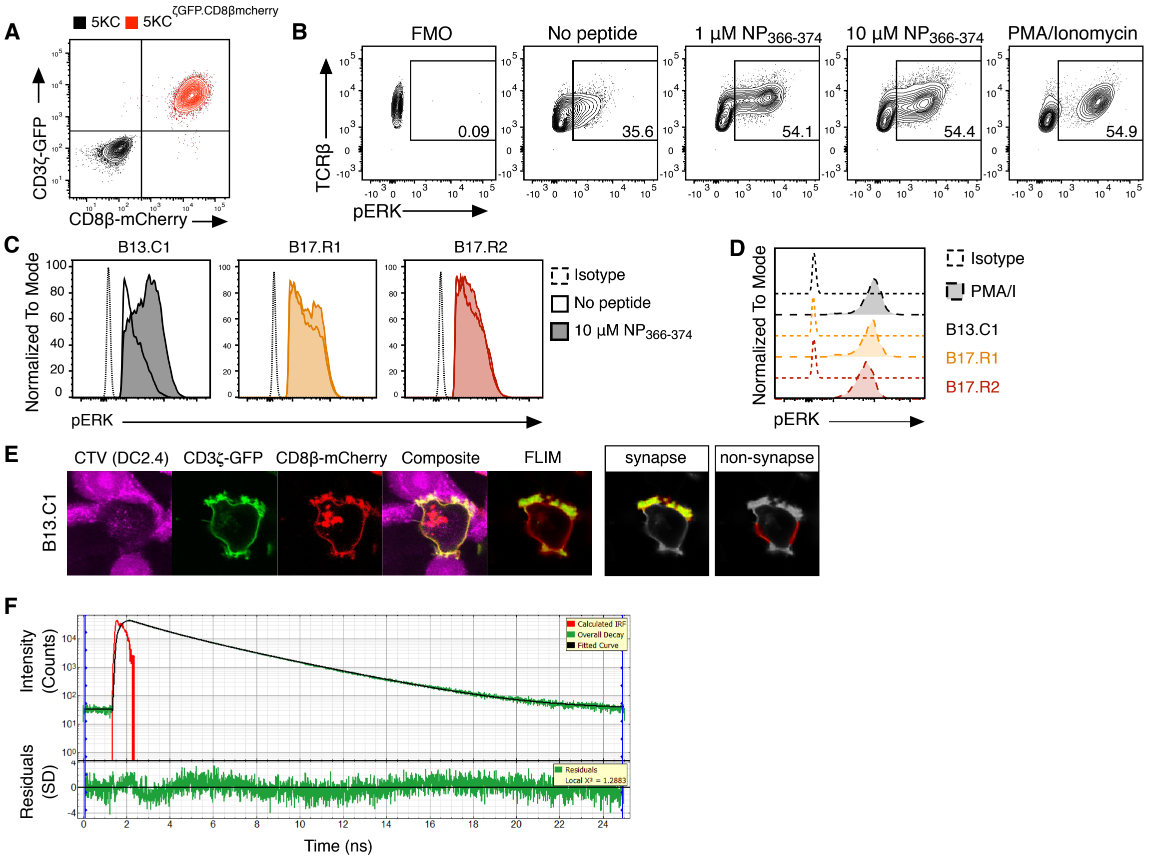

Fig. S3. Sensitivity to stimulation and synapse definition of 5KC$^{\zeta GFP.CD8\beta mcherry}$ cells

The 5KC$^{\zeta GFP.CD8\beta mCherry}$ lines were generated as described (see Methods). (**A**) Overlaid dotplot of the 5KC$^{\zeta GFP.CD8\beta mCherry}$ cell line expressing CD3ζ-GFP and CD8β-mCherry fusion proteins (red) and untransduced 5KC (black). (**B**) B13.C1 TCR^{+} transduced 5KC$^{\zeta GFP.CD8\beta mcherry}$ lines were co-cultured with DC2.4 cells pulsed with medium only, 1 µM or 10 µM of NP$_{366}$ peptide, for 10 minutes before analysis of pERK as described (see Methods). A PMA/Ionomycin control was included as a positive control for pERK staining. (**C**) Representative histograms of pERK expression by TCRβ^{+} pERK^{+} 5KC$^{\zeta GFP.CD8\beta mCherry}$ lines expressing B13.C1 or B17.R2 TCR after co-incubation with DC2.4 cells pulsed with medium only or 10 µM of NP$_{366}$ peptide. (**D**) Representative histograms of pERK expression of each cell line after stimulation with PMA/Ionomycin for 10 minutes. (**E**) CellTrace labelled DC2.4 cells were pulsed with 10 μM of NP_{366} peptide for 1 hour before co-culture with $5KC^{\zeta GFP.\alpha\beta mCherry}$ expressing B13.C1 as a representative sample. T cell lines interacting with a DC2.4 cell were imaged by confocal microscopy up to 20 minutes post co-culture and analyzed by FLIM to measure GFP lifetime (left panel). Shown is a representative image as per **Fig. 5F**. The change in GFP lifetime at the synapse ($Syn\Delta\tau_{AvAmp}$) was calculated by determining τ_{AvAmp} at the synapse by specifying a region of interest (ROI) in Symphotime 64 (PicoQuant) that corresponds to areas of T cell – DC interaction (synapse) or no interaction (non-synapse). Shown is a FLIM-FRET image of a B13.C1 TCR^+ cell as per the left panel to illustrate the representative strategy for identifying synaptic vs. non-synaptic ROI (right panel). (**F**) For analysis of FLIM, TCSPC decay curves were fitted to a bi-exponential reconvolution decay model in SymphoTime 64 to determine donor (GFP) lifetime. A good bi-exponential reconvolution decay curve fit is characterised by X^2 values close to 1 and a representative decay curve is shown in **F.**

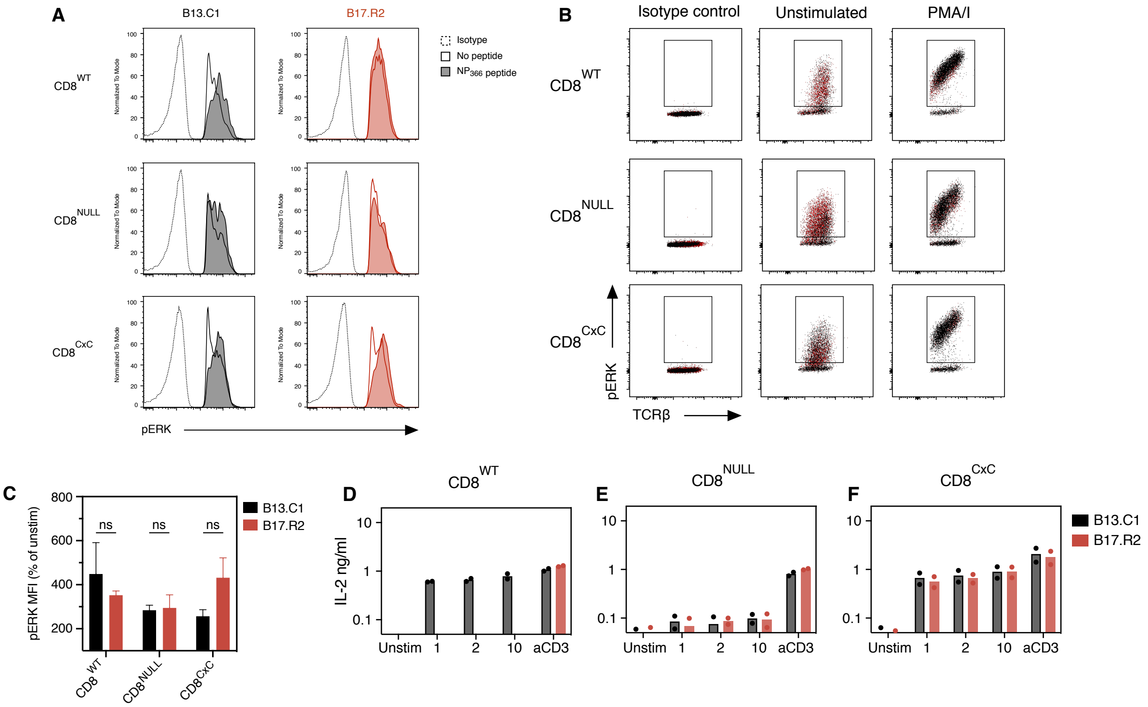

Fig. S4. Responsiveness of T cell lines to PMA/Ionomycin, peptide-pulsed DCs and anti-CD3 Ab stimulation.

(**A**) pERK induction after 10 min stimulation with peptide-pulsed DC2.4 cells was measured by flow cytometry. Shown are representative histograms of CD8^{WT} (top panel), CD8^{NULL} (middle panel) and CD8^{CxC} (bottom panel) from one experiment representative of 3 independent experiments. (**B** and **C**) pERK induction was measured by flow cytometry after 10 min stimulation with PMA (50 ng/mL) and ionomycin (500 ng/mL). (**B**) Representative dot plots showing pERK and TCRβ expression on unstimulated or PMA/ionomycin stimulated CD8^{WT} (top panel), CD8^{NULL} (middle panel) and CD8^{CxC} (bottom panel) cells. (**C**) pERK MFI was normalized to baseline (unstimulated control) to allow the combination of multiple experiments. Samples were tested in duplicate (n=5) and mean and SEM of all datasets shown. Statistical analyses were performed using a paired samples t-test to pair by dataset; ns denotes not statistically significant *P*>0.05. (**D** to **F**) IL-2 secretion by (**D**) CD8^{WT}, (**E**) CD8^{NULL} and (**F**) CD8^{CxC} cells expressing either B13.C1 TCR or B17.R2 TCR was measured by ELISA after 16 h of co-incubation with peptide pulsed DC2.4 cells (1 μM, 2 μM or 10 μM) or antibody-mediated polyclonal stimulation (aCD3). Shown are the means of the absolute IL-2 concentration (before normalization) from one analysis of duplicate samples (n=3).

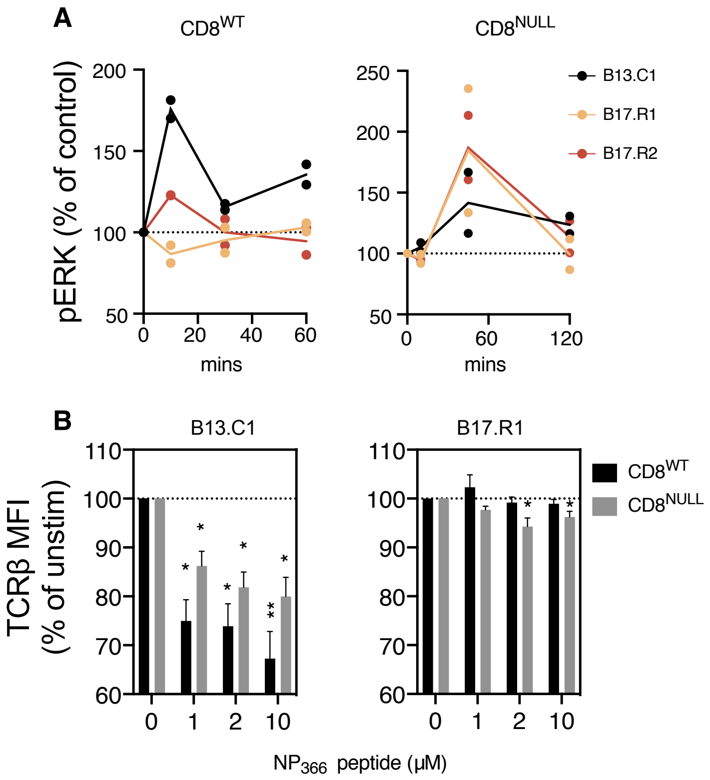

Fig. S5. pERK and TCRβ downregulation for cells expressing canonical and reversed TCRs

(**A**) Time resolved pERK induction (top panels) in cells expressing CD8 (CD8^{WT}, left panel) or lacking CD8 (CD8^{NULL}, right panel) up to 120 min after co-incubation with NP$_{366}$ peptide-pulsed DC2.4 cells, relative to no peptide control (measured at corresponding time point). Shown is each data point and the mean from 2 independent experiments. (**B**) TCRβ downregulation after co-incubation of CD8^{WT} (black bars) or CD8^{NULL} (grey bars) with peptide pulsed DC2.4 cells for 16 hours. Samples were tested in duplicate (n=2) and the mean and SEM of all datasets shown. Statistical analyses were performed using a paired samples t-test to pair by dataset. Statistical significance compared to the no peptide control is indicated by; * $P \leq 0.05$, ** $P \leq 0.01$ as shown.

Table S1. Data collection and refinement statistics

	B17.R2–H-2D^{b}NP$_{366}$	**B17.C1–H-2D^{b}NP$_{366}$**
Data Collection		
Space group	I 2 2 2	C 2 2 2_1
Cell dimensions		
a, b, c (Å)	91.67, 141.00, 217.65	61.77, 224.64, 172.36
α, β, γ (°)	90, 90, 90	90, 90, 90
Number of reflections	56246 (5562)	37844 (3656)
Number of unique reflections	28123 (2781)	19228 (1862)
Resolution (Å)	43.07 – 3.02 (3.13 – 3.02)	43.09 – 3.25 (3.37 – 3.25)
Multiplicity	2.0 (2.0)	2.0 (2.0)
Completeness (%)	100 (100)	99 (100)
I/σ(I)	11.5 (1.8)	13.9 (1.7)
R_{merge}	0.060 (0.367)	0.034 (0.483)
$CC_{1/2}$(%)	99.5 (83.0)	100 (70.1)
Refinement		
No. reflections	28105 (1411 in test set)	19215 (952 in test set)
R_{work} (%)	23.9 (25.0)	27.6 (29.1)
R_{free} (%)	28.1 (29.5)	30.6 (32.1)
Protein residues	828	811
R.m.s deviations		
Bond lengths (Å)	0.01	0.007

Bond angles (°)	1.42	1.13
Ramachandran statistics		
Favored regions (%)	96	94
Allowed regions (%)	3.8	4.9
Outliers (%)	0.37	0.77

Statistics for the highest-resolution shell are shown in parentheses.

Table S2. B17.C1 TCR contacts with H-2D^{b}NP$_{366}$

	B17.C1		
NP$_{366}$ residue	**TCR gene**	**TCR residues**	**Bond type**
Glu4-Oε1- Oε2	CDR1α, CDR3β	Arg37α- Nη1-Nη2, Ser113β	VDW, SB
Met6	CDR1β, CDR2β	Asp37β, Gly109β,Thr115β	VDW
Glu7- Oε1-Oε2	CDR3β	Arg108β-Nη1-Nε	VDW, SB
Thr8- Oγ1	CDR1β	Asp37β-Oδ2	VDW, HB
H2D^{b} residue	**TCR gene**	**TCR residues**	**Bond type**
Glu58-Oε1-Oε2	CDR1α, FWα	Thr28α, Arg86α- Nη1-Nη2	VDW, SB
Gln65-Oε1	CDR3α, CDR3β	Thr109α-O, Gly110α-O, Asn111α-Oδ1, His112β	VDW, HB
Lys66	CDR1α	Arg37α	VDW
Lys68	CDR3β	His112β	VDW
Gly69	CDR3β	Thr110β, His112β	VDW
Gln72	CDR2β	Tyr57β	VDW
Trp73	CDR2β	Tyr57β	VDW
Val76	CDR2β	Tyr57β, Asp58β, Ile64β	VDW
Gly151	CDR3β	Arg108β	VDW

VDW: Van der Waals interaction (cut-off at 4 Å), HB: hydrogen bond (cut-off at 3.5 Å), SB: salt bridge (cut-off at 5 Å).

Table S3. B17.R2 TCR contacts with H-2D^{b}NP$_{366}$

	B17.R2		
Peptide residue	**TCR gene**	**TCR residues**	**Bond type**
Glu4-Oε1	CDR2β	Lys59β-Nζ	VDW, HB
Met6	CDR2β	Ile60β	VDW
Glu7- Oε1-Oε2	CDR2β, FWβ	Leu61β, Arg67β-Nη2-Nε	VDW, SB
Thr8-N- Oγ1	CDR2β, FWβ	Ile60β, Leu61β-O, Asn66β- Oδ1	VDW, HB
H2Db residue	**TCR gene**	**TCR residues**	**Bond type**
Gly16	CDR3α	Thr109α	VDW
Leu17	CDR3α	Thr109α	VDW
Glu18- Oε2	CDR3α	Thr109α, Ser112α-Oγ	VDW, HB
Gly69	CDR2β	Ile60β	VDW
Gln72	CDR2β, CDR3β	Tyr57β, Leu110β	VDW
Trp73	CDR2β	Ile60β	VDW
Arg75-Nη1-Nη2	CDR3α, CDR3β	Ser112α- Oγ, Trp113α, Leu110β-O	VDW, HB
Val76	CDR3α, CDR2β, FWβ, CDR3β	Trp113α, Phe55β, Asn66β, Leu110β	VDW
Arg79-Nη1-Nη2	CDR3α, FWβ	Ala111α,Trp113α,Gln114α- Oε1, Glu68β- Oε1-Oε2	VDW, SB, HB
Asn80-Nδ2	FWβ	Asn66β-Oδ1	VDW, HB
Ala89	CDR3α	Ser110α	VDW

Ile142	FWβ	Phe73β	VDW
Arg145-Nη2	FWβ	Phe73β, Glu74β-Oε1	VDW, HB
Lys146-O- Nζ	FWβ	Arg67β-O- Nη2, Phe73β	VDW, HB
Gln149- Oε1	FWβ	Arg67β- Nη1, Phe73β-O-Glu74, Gln77	VDW, HB

VDW: Van der Waals interaction (cut-off at 4 Å), HB: hydrogen bond (cut-off at 3.5 Å), SB: salt bridge (cut-off at 5 Å).

Table S4. Ternary complex statistics compared with other TCR-pMHCI

TCR	**Peptide/ MHC**	**BSA**	**Vα**	**Vβ**	**peptide**	**1α**	**2α**	**3α**	**FWα**	**1β**	**2β**	**3β**	**FWβ**	**K$_D$ (μM)**	**Angle (º)**
B17.C1	H2D^{b}NP$_{366}$	1575	25	75	33	14.4	0	7	3.7	13.8	23.2	37.8	0	>>200	33
B17.R2	H2D^{b}NP$_{366}$	1860	26.4	73.6	18.9	0.1	0	26.3	0	0	27.3	7.1	39.2	6.34	238
Literature	Average value	1910	52	47.5	28.9	16	11.6	20.3		7.2	11.9	23.9		35	63.2
	Smallest value	1240	33	22	17	3.5	5.1	4.6		0	0	8.3		0.3	37
	Largest value	2400	78	67	48.6	28.7	19.7	34.7		19.2	33.3	42		278	90

BSA: Buried Surface Area (Å^2) total calculated with AreaIMol (CCP4), Vα: contribution of the α-chain to the TCR BSA in %, Vβ contribution of the β-chain to the TCR BSA in %, 1α represent the BSA contribution of the CDR1α loop as a % of the TCR BSA (same for the 2α: CDR2α, 3α: CDR3α, 1β: CDR1β, 2β: CDR2β and 3β: CDR3β). The K$_D$ represent the affinity reported in μM, angle represent the docking of the variable domains angle in degrees. The average, lowest and highest values from the literature are represented in the grey section at the bottom of the table for an easy comparison (*1*).